Leveraging autophagy and pyrimidine metabolism to target pancreatic cancer

Suzanne Dufresne[1], Ramya S. Kuna[1], Kristiana Wong[1,2], Anvita Komarla[1,3], Louis R. Parham[1], Celina Shen[1,2], Payel Mondal[1], Adelaida Estrada-Cardenas[1,2], Angelica Rock[1,2], Joel Encarnación-Rosado[1], Fabiana Izidro Layng[4], Dhanya R. Panickar[4], Nicole A. Bakas[4], Douglas J. Sheffler[4], Allison Limpert[4], Kristina L. Peck[5], Alexandra Fowler[5], Sonja N. Brun[1], Tammy J. Rymoff[1], Andrew M. Lowy[6], Dannielle D. Engle[5], Hervé Tiriac[6], Reuben J. Shaw[1], Nicholas D. P. Cosford[4], Christian M. Metallo[1,2,3], Christina G. Towers[1,2*]

[1]Molecular and Cell Biology Laboratory, Salk Institute for Biological Studies, La Jolla, CA 92037, USA.

[2]Division of Biological Sciences, University of California San Diego, La Jolla, CA 92037, USA.

[3]Department of Bioengineering, University of California San Diego, La Jolla, CA 92037, USA.

[4]Center for Therapeutics Discovery, NCI-Designated Cancer Center, Sanford Burnham Prebys Medical Discovery Institute, La Jolla, CA 92037, USA

[5]Regulatory Biology Laboratory, Salk Institute for Biological Studies, La Jolla, CA 92037, USA.

[6]Department of Surgery, Division of Surgical Oncology, Moores Cancer Center, University of California San Diego, La Jolla, CA 92037, USA

[*]Lead Contact: For correspondence, please contact Christina Towers at CTowers@Salk.edu

SUMMARY

Autophagy inhibitors are promising compounds to treat pancreatic ductal adenocarcinoma (PDA) but their efficacy in patients is unclear, highlighting a need to understand mechanisms of resistance. We uncovered metabolic adaptations that bypass autophagy inhibition. Utilizing PDA cells with acquired resistance to different autophagy inhibitors, we found that severe autophagy depletion induces metabolic rewiring to sustain TCA intermediates and nucleotides for biosynthesis. Long-term autophagy inhibition results in decreased pyruvate decarboxylation and increased pyruvate anaplerosis, likely regulated by lower pyrimidine pools. Cells adapting to autophagy inhibition increase pyrimidine salvage to replenish these pools instead of synthesizing them de novo. Exploiting this metabolic vulnerability, we found that acquired resistance to autophagy inhibition promotes increased pyrimidine salvage and therefore sensitivity to pyrimidine analogues, including gemcitabine and trifluridine/tipiracil, leading to combinatory effects with autophagy inhibitors and pyrimidine analogs. These studies provide mechanistic insight defining how autophagy inhibition can be leveraged to treat PDA.

KEY WORDS

Autophagy, drug resistance, pyruvate metabolism, pyrimidine metabolism, gemcitabine, lysosomes, hydroxychloroquine, ULK1, pancreatic cancer, nucleotides

INTRODUCTION

Pancreatic ductal adenocarcinoma (PDA) is a highly aggressive form of pancreatic cancer with limited treatment options. This devastating disease undergoes heavy metabolic rewiring throughout tumor progression and in response to treatment. There have been many efforts to leverage metabolic vulnerabilities into better therapeutic strategies, although thus far with little clinical success.

Over the past decade, the cellular recycling process, autophagy, has emerged as a promising therapeutic target for this disease[1–4]. Autophagy is a catabolic process that degrades and recycles damaged cellular material by trafficking cargoes to the lysosome[5–7]. As a coordinated stress response, autophagy maintains metabolic homeostasis, protein turnover, and organelle quality control – thereby supporting cancer cell survival. Oncogene activation, including *KRAS* mutations – present in more than 90% of PDA, increases autophagy levels[8–10] to provide a survival advantage in nutrient-deprived and hypoxic conditions characteristic of pancreatic cancer[11]. Autophagy-mediated recycling provides a variety of substrates to fuel nearly all aspects of central carbon metabolism[12,13,10,14–18]. In addition, autophagy recycles nucleic acids into nucleotide building blocks to preserve nucleotide homeostasis[19–22], a necessary metabolic trait for the maintenance of high proliferative rates of PDA cells[23].

Numerous studies have shown that perturbation of autophagy decreases PDA cell survival across in vitro and in vivo models. For example, deletion of the core autophagy gene *Atg5* or expression of a dominant negative mutant of *Atg4b* in the classic *Kras*$^{LSL\text{-}G12D/+}$, *Tp53*$^{flox/+}$, *Pdx1-Cre* (KPC) PDA model results in slower tumor growth and increased survival[24,25]. Therefore, autophagy represents an attractive potential target for this devastating disease. Chloroquine (CQ) and hydroxychloroquine (HCQ) are FDA-approved drugs, initially used to treat malaria, that block autophagy and lysosomal function. Although chloroquine derivatives are potent autophagy inhibitors in cultured cells, low in vivo bioavailability along with low specificity limit their therapeutic

potential. Therefore, recent efforts have led to the development of more specific autophagy inhibitors including compounds that target the upstream Unc-51 Like Autophagy Activating Kinases 1 and 2 (ULK1/2)[26–31] as well as other autophagy-regulating enzymes [32–34].

Over 60 clinical trials have launched combining CQ or HCQ with standard of care therapies for the treatment of various types of cancer[35]. Despite promising preclinical findings, the results from clinical trials have been disappointing, likely caused by a compilation of inherent and acquired therapeutic resistance along with inadequate drug bioavailability[36]. This is supported by previous findings from our lab showing that lung and breast cancer cells that are initially dependent on autophagy and sensitive to genetic deletion of core autophagy genes like *ATG7* or *RB1CC1* (*FIP200*) can adapt over time and become autophagy-independent[37,38]. However, whether PDA cells can acquire resistance to pharmacological blockade of autophagy inhibition remains unknown. Prior studies have explored different drug combinations that could improve autophagy inhibition to treat PDA including targeted inhibition of the MAP Kinase pathway [39,40,33,34], insulin like growth factor 1 receptor (IGF1R)[41], sphingolipid metabolism[42], and autophagy related processes like macropinocytosis[43], each demonstrating increased efficacy over single agent use of autophagy inhibitors. Nonetheless, these efforts have not yet resulted in better, clinically relevant, therapeutic strategies to target autophagy in PDA.

In this study, we took a unique approach to investigate the metabolic alterations and adaptations PDA cells use to acquire resistance to autophagy inhibitors. For the first time, we generated PDA cells resistant to either the lysosomal inhibitor, HCQ, or the ULK1/2 inhibitor, MRT68921. Cells with acquired resistance maintain autophagy inhibition but undergo metabolic rewiring to adapt and survive. The resistant cells have altered pyruvate metabolism and pyrimidine synthesis, resulting in increased pyrimidine salvage. We exploited this vulnerability and found that acquired resistance to autophagy inhibitors resulted in increased salvage of pyrimidine analogues and therefore a dramatic sensitivity to the PDA standard-of-care drug, gemcitabine, as well other clinically relevant pyrimidine analogues like the thymidine analogue

trifluridine. Together, our findings provide mechanistic insight into metabolic alterations that occur in response to autophagy inhibition and indicate that combining autophagy inhibitors and pyrimidine analogs represents a promising therapeutic strategy for PDA.

RESULTS

PDA cells that acquire resistance to autophagy inhibition have blocked autophagy

To interrogate if and how PDA cells acquire resistance to pharmacological autophagy inhibition, we used murine PDA cell lines derived from the well-established KPC mouse model including FC1199 (male), FC1245 (female) cells, as well as the human PDA cell line MIA PaCa-2. The cells were exposed to increasing doses of the autophagy inhibitor hydroxychloroquine (HCQ) or the ULK1/2 kinase inhibitor MRT68921 (MRT) (Figure 1A). Cell viability assays confirmed that cells exposed to HCQ or MRT6891 had a 5-6 fold increase in IC50 dose (hereafter termed HCQ-R or MRT-R, respectively), compared to CTL cells passaged alongside the resistant cells (Figure 1B-E, S1A-D). Cell proliferation assays using Incucyte live-cell imaging and colony formation assays confirmed resistance where CTL cells showed a robust decrease in proliferation when exposed to HCQ or MRT, while the HCQ-R and MRT-R cells showed no change in viability (Figure 1F-G, S1E-G). The resistant cell lines actively proliferate while in drug, but their basal growth rates are slightly slower than their matched CTL counterparts.

To determine if autophagy is blocked in the HCQ-R and MRT-R cells, autophagy flux was assessed using the mCherry-GFP-LC3 tandem fluorescent reporter[44,45]. GFP is pH sensitive, and the fluorescence is quenched in the lysosome, whereas mCherry is pH stable. Ratiometric flow cytometry can be used to quantify the ratio of mCherry over GFP as a direct measure of autophagic flux. After expressing mCherry-GFP-LC3 in CTL, HCQ-R and MRT-R cells, we found the CTL cells responded to 24hr amino acid starvation in EBSS with a robust increase in

autophagic flux. However, the HCQ-R and MRT-R cells were unable to induce autophagy in these conditions (Figure 1H-I). We confirmed that autophagy flux is decreased in the resistant cells using autophagy flux assays via immunoblotting for LC3 after treatment with the lysosome inhibitor Bafilomycin A1 (BafA1) highlighting that adaptation to the autophagy inhibitors does not reinstate autophagic flux (Figure S1H-J).

Cell viability and clonogenic assays revealed that the HCQ-R cells are also resistant to MRT68921 and that MRT-R cells are resistant to HCQ. Moreover, both HCQ-R and MRT-R cells are resistant to other autophagy inhibitors including the chloroquine derivative, DC661, and the lysosome inhibitor, BafA1 (Figure 1J-U, S1G, S1K-L). While both HCQ and MRT68921 have some off-target effects, these results show that the acquired resistance is on-target and autophagy is impaired in the HCQ-R and MRT-R cells. Importantly, the resistant cells proliferate indicating that they have adapted to bypass autophagy.

PDA cells resistant to autophagy inhibition rewire their metabolism and decrease pyruvate decarboxylation

To assess the modifications necessary to bypass pharmacological blockade of autophagy, we performed RNA sequencing on the autophagy inhibition resistant FC1199 cells and drug naïve CTL cells. We compared differentially expressed genes (DEGs) and the corresponding Gene Ontology (GO) pathways from the two resistant cell line lines along with autophagy deficient *Atg7* KO cells (as a positive control for autophagy-inhibited pathways). There was a significant overlap in altered pathways suggesting that some mechanisms of resistance are shared between all three cell lines (Figure S2A-D). Within these shared GO terms, numerous metabolism-related pathways were altered, both positively and negatively (Figure 2A-B). To better discern the metabolic changes in the resistant cells, we performed metabolomic assays with gas chromatography-mass spectrometry (GC-MS). HCQ-R and MRT-R cells showed significantly higher levels of pyruvate,

but decreased citrate and α-ketoglutarate (α-KG) levels compared to drug naïve CTL cells (Figure 2C-F, Figure S2E-P). Moreover, the HCQ-R cells had increased aspartate (Figure 2C).

These results suggest altered pyruvate dehydrogenase complex (PDH) function in the resistant cells. Once imported into mitochondria, glycolytic-derived pyruvate can undergo pyruvate decarboxylation via PDH to form acetyl-CoA. Acetyl-CoA then condensates with oxaloacetate (OAA) to generate citrate which enters the tricarboxylic acid (TCA) cycle. In the presence of [U-$^{13}C_6$] glucose, M3 pyruvate undergoes pyruvate decarboxylation leading to M2 citrate (Figure 2D). We found a decrease in the M2 Citrate over M3 Pyruvate ratio in the resistant cells (Figure 2E-G, Figure S2E-L), indicative of decreased pyruvate decarboxylation. Datamining gene expression across human PDA cell lines through Depmap also revealed a positive correlation between gene signatures related to autophagy and PDH regulation[46,47] (Figure 2H).

Given these alterations in pyruvate metabolism, a process largely isolated to the mitochondria, we assessed mitochondrial function more broadly. Seahorse assays were performed to measure oxygen consumption rates (OCR) as a proxy for oxidative phosphorylation and revealed that the HCQ-R and MRT-R cells have defective mitochondria that cannot reach the same maximal respiration as the CTL cells (Figure 2I-K). Similar results were seen in FC1245 cells with acquired resistance to autophagy inhibition (Figure S3A).

To further characterize TCA function alterations, we performed a [U-$^{13}C_5$] glutamine trace, as glutamine is a key anaplerotic substrate that replenishes TCA cycle intermediates (Figure S3B). We found that glutamine utilization in the TCA cycle was significantly reduced in the HCQ-R cells compared to drug naïve CTL cells, indicated by decreased M5 α-KG, M4 fumarate, M4 malate, M4 aspartate and M4 citrate (Figure S3B-L). Together, these findings confirm that the TCA function is altered in autophagy inhibition resistant cells as glucose and glutamine utilization is decreased in the resistant cells compared to controls.

PDA cells resistant to autophagy inhibition undergo anaplerosis to limit TCA dysfunctions

Surprisingly, the resistant cells have equal oxygen consumption rates under basal conditions suggesting the mitochondria are relatively functional, in the absence of stress (Figure 2J). This, coupled with the fact that resistant cells are actively proliferating, indicates the cells can circumvent decreased pyruvate decarboxylation to sustain TCA metabolism. Since incorporation of glutamine-derived carbons into the TCA cycle is reduced in autophagy inhibition resistant cells, we asked whether TCA intermediates could be replenished by additional anaplerotic reactions. In the [U-$^{13}C_5$] glutamine trace, we observed a modest but significant increase in M5 citrate in HCQ-R cells compared to controls, indicative of a slight increase in reductive carboxylation (Figure S3K-L).

Another major anaplerotic pathway used to replenish TCA intermediates is pyruvate carboxylation. Besides PDH-mediated pyruvate decarboxylation, the other major fate of glycolytic pyruvate is pyruvate carboxylation (PC) via the rate limiting enzyme pyruvate carboxylase (PCx), resulting in the conversion of pyruvate to oxaloacetate[48]. A [U-$^{13}C_6$] glucose trace revealed an increase in M3 fumarate, M3 malate, and M3 aspartate suggesting the resistant cells have increased pyruvate anaplerosis through PC (Figure 3A-S). To validate this, we used a positional tracer, [3-$^{13}C_1$] glucose, where only the third carbon of glucose is labelled and ^{13}C is lost in the PDH reaction and only retained through the PC reaction resulting in M1 malate and M1 aspartate (Figure 3T). Using this tracer, we found that the autophagy inhibition resistant cells have increased M1 aspartate and M1 malate over M1 pyruvate compared to drug naïve CTL cells (Figure 3U-V and Figure S3M-O). Further supporting these results, PCx is upregulated at both the transcript (*Pcx* gene) and protein level in the HCQ-R and MRT-R cells (Figure 3W-X). Together, these results show that PDA cells that adapt to autophagy inhibition have altered TCA metabolism and glutamine anaplerosis. However, the resistant cells can compensate by increasing reductive carboxylation and PC to replenish TCA intermediates.

PDA cells resistant to autophagy inhibition have decreased nucleotide pools and altered pyrimidine metabolism

Recently, Sahu et al.[49] found that lower pyruvate decarboxylation can be caused by decreased pyrimidines, one of the two families of nucleotides that make up nucleic acids. UTP is the main phosphodonor for the phosphorylation of thiamine into thiamine pyrophosphate (TPP) by thiamine pyrophosphokinase 1 (TPK1), and TPP positively regulates PDH activity[49]. Therefore, low UTP causes a decrease in TPK1 activity, effectively reducing PDH-mediated pyruvate decarboxylation (Figure 4A). Interestingly, *Tpk1* mRNA and protein expression were significantly decreased in HCQ-R and MRT-R cells compared to drug naïve CTL cells (Figure 4B-C). Furthermore, gene set enrichment analyses (GSEA) on DEGs from RNA-seq showed that nucleotide metabolism and particularly pyrimidine metabolism-related pathways were significantly altered in HCR and MRT-R cells compared to drug-naïve CTL cells (Figure 4D). Liquid chromatography-mass spectrometry (LC-MS) revealed that some nucleotides, in particular several pyrimidine pools, were decreased in the HCQ-R and MRT-R cells, with less significant changes observed in purine pools (Figure 4E-F, S4A-B). If the resistant cell lines have altered free pyrimidine pools, but are still actively proliferating, we reasoned that they must utilize pyrimidine metabolism pathways to generate and incorporate pyrimidines into the critical biomass of RNA and DNA.

Most cells can synthesize pyrimidines from aspartate and also salvage pyrimidines. The rate limiting enzymes for the de novo pyrimidine synthesis pathway are Carbamoyl-phosphate synthetase 2, Aspartate transcarbamoylase, and Dihydroorotase (CAD) and dihydroorotate dehydrogenase (DHODH)[50,51]. On the other hand, pyrimidine salvage recovers extracellular nucleosides and nucleobases from the extracellular environment or from intracellular nucleic acid degradation to synthesize nucleotides[50,51]. Extracellular pyrimidines are transported into the cell through ENT/SLC29 and CNT/SLC28 nucleoside transporters and then converted into their corresponding nucleoside monophosphates through phosphorylation reactions, including

deoxycytidine kinase (dCK) and thymidine kinase (TK1)[50,52] (Figure 4G). We found that the HCQ-R and MRT-R resistant cell lines have decreased expression in the rate-limiting enzymes for the de novo synthesis pathway but increased expression in pyrimidine salvage enzymes and transporters (Figure 4H, S4C-F). A [α-^{15}N] glutamine trace revealed that while there was a small increase in M1 labeling on some pyrimidines, i.e. UMP and UDP, but not on others, i.e. CTP (Figure S4G-J), there was also a similar increase in M1 aspartate, the precursor metabolite for the DHODH reaction (Figure S4K). Quantification of M1 labeled nucleotides to M1 aspartate revealed no differences between CTL and resistant cells (Figure S4L-N) indicating the resistant cells are unable to maximize the available aspartate to replenish all pyrimidine pools, likely a result of decreased DHODH and CAD. Together these data indicate that de novo pyrimidine synthesis is not sufficient to maintain pyrimidine pools and several pyrimidines remain low (Figure 4E-F).

Depletion of DHODH, a context previously shown to decrease pyrimidine pools[53,49,54,52,51], increased expression of dCK (Figure 4I), suggesting that low pyrimidine pools is sufficient to trigger increased pyrimidine salvage protein expression. Therefore, we propose that low pyrimidine pools drive increased pyrimidine salvage in the cells with acquired resistance to autophagy inhibition.

PDA cells resistant to autophagy inhibition have increased sensitivity to pyrimidine analogs

Considering that the HCQ-R and MRT-R cell lines upregulate the pyrimidine salvage pathway, we hypothesized that the resistant cells also increase the salvage of pyrimidine analogues through this same pathway. Cell viability assays in the HCQ-R, MRT-R, and CTL cells treated with a panel of drugs including current PDA standard of care, and targeted agents tested in clinical trials, including pyrimidine analogs revealed pan-resistance to most compounds except for pyrimidine analogs, including gemcitabine (2′,2′-difluorodeoxycytidine), FTD/TPI (5-trifluromethyl-

2'-deoxyuridine combined with stabilizing agent tipiracil), and cytarabine (another cytidine analogue with a modified sugar moiety; 1-.beta.-D-arabinofuranosyl-4-amino-2(1H)pyrimidinone) (Figure 5A-C). Interestingly, fluorouracil (5-FU; 5-fluoro-2,4-(1H,3H)-pyrimidinedione) is also considered a pyrimidine analogue, however it is metabolized through the de novo pyrimidine synthesis pathway[55,56], unlike gemcitabine, FTD/TPI, and cytarabine – all of which are which are metabolized through the pyrimidine salvage pathway. Accordingly, the HCQ-R and MRT-R cells are not more sensitive to 5-FU (Figure 5A-B). Moreover, the HCQ-R and MRT-R cells are not more sensitive to small molecules that target de novo pyrimidine metabolism via DHODH like Brequinar or BAY-2402234 (Figure S4O-R).

Gemcitabine and FTD/TPI are of particular interest because they are in widespread clinical use. Gemcitabine is an FDA standard-of-care agent for PDA treatment and FTD/TPI is used for colorectal and gastric cancers[57–59]. FTD/TPI is currently being tested in clinical trials for PDA patients in combination with paclitaxel (NCT04046887). The HCQ-R and MRT-R cells have a 3-5-fold decrease in the IC50 for gemcitabine and FTD/TPI (Figure 5A-B, 5D-M). Similarly, the FC1245 and MIA PaCa-2 cells with acquired resistance to autophagy inhibition are also hypersensitive to these pyrimidine analogues (Figure S5A-G). Incucyte live-cell imaging confirmed that low doses of gemcitabine and FTD/TPI, that have minimal effects in the CTL cells, drastically limit cell growth in the HCQ-R and MRT-R lines (Figure 5H, 5M, S5E).

Gemcitabine incorporation into DNA interferes with DNA synthesis and inhibits cell proliferation. Gemcitabine also inhibits ribonucleotide reductase (RNR), which catalyzes the formation of deoxyribonucleotides[60,61]. To assess if gemcitabine sensitivity is due to increased salvage because it resembles a pyrimidine or because it targets RNR, we tested the effects of another small molecule, triapine – a thiosemicarbazone, that also targets RNR, but is not a pyrimidine analogue[62]. Interestingly, the FC1199 and FC1245 HCQ-R and MRT-R cells are resistant to triapine indicating the pyrimidine structure of gemcitabine is likely necessary for its increased uptake in the autophagy-inhibitor-resistant cells (Figure S5H-K). Since we

hypothesized that low pyrimidine pools drive the increase in pyrimidine salvage and enhance sensitivity to pyrimidine analogs, we tested if limiting pyrimidine pools, via DHODH loss and uridine deprivation, would be sufficient to drive increased sensitivity to pyrimidine analogues. Indeed, cell viability assays showed that loss of DHODH increased sensitivity to gemcitabine which could be rescued with the addition of uridine (Figure 5N-O).

To further explore if the increased sensitivity to these compounds is due to increased salvage in the resistant cells, we tested if the addition of extracellular pyrimidines could rescue these effects. The addition of deoxycytidine or uridine abrogated the increased sensitivity to gemcitabine in the FC1199 and FC1245 HCQ-R cells (Figure 5P, S5L-M). Similar effects were found in FC1199 MRT-R cells treated with FTD/TPI, and the effects could be rescued with the addition of either thymidine or uridine (Figure 5Q, S5N). Interestingly, the fact that uridine phenocopies deoxycytidine/thymidine in these assays indicates that the low intracellular pyrimidine pools are leading to a broad upregulation of pyrimidine salvage. Uridine can restore CMP and TMP levels in cells – since uridine-derived UMP is readily converted to these other pyrimidines – thereby rescuing sensitivity to pyrimidine analogues.

Prior studies found that *dCK* and *TK1* expression correlate with sensitivity to the deoxycytidine analogue, gemcitabine[63–66], and the thymidine analogue, trifluridine[67,68], respectively. To determine if upregulated salvage proteins is necessary for the observed sensitivity to pyrimidine analogues, we used CRISPR/Cas9 guide RNAs to deplete dCK, the enzyme required to metabolize salvaged pyrimidines as well as gemcitabine. Figure 5R shows that loss of dCK rescues the differential sensitivity between the HCQ-R and CTL cells (Figure 5R, S5O). Together these studies demonstrate that cells that acquire resistance to autophagy inhibition, upregulate pyrimidine salvage, and consequently increase uptake of pyrimidine analogues leading to hypersensitivity.

To determine if this acquired sensitivity to pyrimidine analogues is maintained in vivo we orthotopically transplanted the HCQ-R and CTL cells into the pancreata of C57Bl/6 mice. We first

confirmed that the autophagy-inhibitor-resistant cell lines maintain resistance to autophagy inhibitors and sensitivity to gemcitabine even if they are grown without continuous dosing of the autophagy inhibitors (Figure S5P-U). This allowed us to remove the cells from drug to transplant them in vivo. We injected the FC1245 and FC1199 HCQ-R cells orthotopically in the pancreas and found that a low gemcitabine dose did not impact CTL tumor growth but significantly reduced HCQ-R tumor volume, despite equal tumor size prior to drug treatment (Figure 5S-T, S5V-W).

All together these studies lead us to propose a mechanistic model stating that as cells acquire resistance to autophagy inhibition, they rewire their metabolism. This results in an overall decrease in pyrimidine pools as well as altered TCA metabolism including decreased pyruvate decarboxylation. As a work-around, the resistant cells increase pyruvate anaplerosis to replenish TCA intermediates and generate aspartate to replenish pyrimidine pools. However, since DHODH and de novo pyrimidine metabolism do not also increase to match this need, the cells must salvage pyrimidines from the extracellular environment. This adaptation leads to increased pyrimidine salvage and causes the cells to increase salvage of pyrimidine analogues, resulting in a hypersensitivity to different pyrimidine analogues (Figure 5U).

Autophagy inhibitors and pyrimidine analogues have a combinatory effect in PDA

These new mechanistic insights led us to test the effects of combining autophagy inhibition and pyrimidine analogues. We used a biobank of pharmacotyped PDA patient-derived organoids (PDOs) which represent a translationally relevant model that can predict response to treatment in patients[69]. We compared RNA-seq and sensitivity to gemcitabine in a cohort of 43 PDOs. The original tumor samples were obtained from patients of both sexes (20 women, 23 men), and the majority were derived from the primary PDA, with six derived from metastatic sites and two from ascites. 40 PDO's have *KRAS* mutations (including G12D, G12V, G12R and Q61H) while three maintain WT *KRAS*. We found a significant correlation between the autophagy-lysosome gene

signature[70] and gemcitabine sensitivity across PDOs showing that low autophagy gene expression correlates with higher gemcitabine sensitivity (Figure 6A). When assessing individual autophagy gene expression with gemcitabine sensitivity, we found the most robust correlations with *Ulk1* expression and the *Ulk1* interacting protein, *Atg13* (Figure 6B-C).

We next assessed the effects of combining autophagy inhibitors HCQ or MRT68921 with gemcitabine or FTD/TPI in FC1199, FC1245 and MIA PaCa-2 drug naïve cells. Incucyte live-cell imaging and clonogenic growth assays revealed that all combinations with autophagy inhibitors and pyrimidine analogues resulted in a greater effect on cell viability than any single agent (Figure 6D-H, S6A-J). HCQ has poor bioavailability and specificity, while targeting ULK1/2 kinases may overcome these limitations, representing a more attractive therapeutic strategy. Importantly, MRT68921 showed a robust combinatory effect with both gemcitabine and FTD/TPI resulting in decreased cell survival and increased apoptosis, as measured by cleaved caspase activity with Incucyte live cell imaging (Figure 6D-H, S6F-I). Despite these promising in vitro studies with MRT68921, this drug showed no single agent effect in vivo suggesting it too has poor bioavailability (data not shown).

Shaw et al. have recently designed and synthesized a series of potent small molecule inhibitors of the ULK1/2 kinases, including SBP-1750[71,72,29,31]. These compounds possess good oral bioavailability and exposure, highlighting their potential as promising candidates for combination therapy studies. The compounds bind to the ULK1 and ULK2 kinase domains leading to a robust inhibition of autophagy flux and reduced cell viability across different cancer cell lines. Moreover, these compounds cause a decrease in the ULK1/2 binding partners, ATG13 and ATG101, both in vitro and in vivo demonstrating robust in vivo target engagement[31]. In particular, the compound SBP-1750 leads to more potent ATG13 degradation and inhibits autophagic flux at lower doses compared to other ULK1/2 inhibitors – including the MRT series – and lysosome inhibitors like HCQ. Moreover, SBP-1750 kills cancer cells in vitro and shows single-agent effect

on reducing tumor growth in orthotopic PDA models in vivo. Most importantly, SBP-1750 has good bioavailability in mice resulting in ATG13 degradation in vivo with minimal dose toxicities[73].

Since we observed a robust correlation with both *ULK1* and *ATG13* expression with gemcitabine across PDOs (Figure 6B-C), we reasoned that a compound like SBP-1750 that targets ULK1 kinase activity and causes a decrease in ATG13 expression would be the most efficacious. Given this, we combined SBP-1750 with pyrimidine analogues and found a robust combinatory effect with both gemcitabine and FTD/TPI (Figure 6I-M). To confirm this effect in vivo, we orthotopically transplanted FC1199 cells into the pancreata of C57Bl/6 mice. This therapeutic strategy did not lead to dose-limiting toxicities (Figure 6N) and combining treatment with SBP-1750 and a low dose of gemcitabine resulted in the most robust decrease in tumor size (Figure 6O-P). Prior studies showed that this series of ULK1/2 inhibitors decreases ATG13 protein expression. Accordingly, target engagement was confirmed via reduced Atg13 protein expression in the tumors (Figure 6Q). Together these studies indicate that targeting autophagy using novel ULK1/2 inhibitors causes altered pyrimidine metabolism which can be leveraged to increase sensitivity to clinically relevant pyrimidine analogues like gemcitabine.

DISCUSSION

Numerous in vitro and physiologically relevant in vivo studies confirm that autophagy is a valid target to treat pancreatic cancer[9,24,10,74,25,16]. However, the field lacked a mechanistic understanding of how autophagy inhibition rewires cell metabolism, resulting in ineffective therapeutic strategies and acquired resistance. In this study, we generated PDA cells resistant to autophagy inhibitors to better understand these acquired adaptations and in the process, we identified unique metabolic vulnerabilities (Figure 1, S1). Through targeted metabolomics we found a novel link between autophagy and pyruvate decarboxylation showing that pyruvate carboxylation can compensate for autophagy-inhibition-induced blockade of pyruvate

decarboxylation via PDH (Figure 2, 3, S2, S3). These results align with previous studies in non-cancer cells with dysfunctional PDH activity (*Pdha1* KO) which also found an increase in PC activity[75,76]. Previous findings also linked autophagy to nucleotide metabolism[21 22]. However, our studies are the first to indicate that autophagy-regulated pyrimidine pools alter pyruvate metabolism.

We show that as cells adapt to autophagy inhibition, they are limited in their ability to utilize de novo pyrimidine synthesis and instead preferentially salvage pyrimidines (Figure 4, S4). We and others have shown that DHODH inhibition is sufficient to phenocopy this result and increase the pyrimidine salvage pathway[77]. Therefore, our results indicate that autophagy inhibition and regulation of DHODH is upstream of increased pyrimidine salvage (Figure 5U). Importantly, this pathway is not only involved in the salvaging of pyrimidines, but also in the metabolism of pyrimidine analogs. One open question is how the pancreas tumor microenvironment (TME) provides pyrimidines for the tumor cells to salvage. Prior studies have shown that both macrophages and fibroblasts can secrete pyrimidines, altering tumor sensitivity to gemcitabine[78,79], suggesting these cells within the TME could be the nucleotide donors.

Instead of trying to thwart resistance to autophagy inhibition, we propose to leverage it. Pyrimidine analogs (i.e., gemcitabine) are commonly used to treat PDA patients but typically show limited efficacy. Our studies show that as the HCQ-R and MRT-R cells upregulate pyrimidine salvage pathways to meet nucleotide demands, these cells also salvage compounds that resemble pyrimidines, i.e. pyrimidine analogues, resulting in increased sensitivity to these compounds, especially the thymidine analog FTD/TPI, as well as the deoxycytidine and cytidine analogues gemcitabine and cytarabine, respectively (Figure 5, S5).

Autophagy-inhibition-induced upregulation of nucleotide salvage and pyrimidine analog uptake may therefore represent a valuable therapeutic leverage for PDA patients, and we found a positive correlation between autophagy gene signatures and gemcitabine sensitivity in human-derived PDOs. We found that combining autophagy inhibitors, HCQ or MRT68921, with

pyrimidine analogues, gemcitabine or FTD/TPI, resulted in a combinatory cell killing effect (Figure 6). Previously, HCQ and gemcitabine were clinically tested in a Phase II randomized clinical trial in PDA patients[36] (NCT01506973). While the results showed an increase in response rate with HCQ, there was no improvement in the primary end point of overall survival at 12 months. This result highlights the need for better autophagy inhibitors to combine with pyrimidine analogues. Our mechanistic studies compare HCQ and ULK1/2 inhibition allowing us to draw the important conclusion that autophagy inhibition, irrespective of where in the pathway, alters pyrimidine metabolism. But HCQ is unlikely to be an effective therapeutic drug in the clinic due to its low specificity and bioavailability. MRT68921 shows increased specificity and bioavailability compared to HCQ but still has limited potency and is unlikely to be tested in the clinical setting in its current form.

More specific autophagy inhibitors, and in particular more potent ULK1/2 inhibitors, are being developed[80] [26]. Targeting ULK1/2 is effective at reducing PDA cell growth[29]. SBP-1750, a newly developed ULK1/2 inhibitor from Shaw et al.[71] exhibits improved bioavailability in mice and oral exposure compared to previously developed ULK1/2 autophagy inhibitors, making it an ideal candidate for our combinatorial studies. We combined SBP-1750 with gemcitabine or FTD/TPI and found a robust combinatory effect on PDA cell viability in vitro and tumor growth in vivo (Figure 6). This result emphasizes that ULK1/2 inhibition combined with pyrimidine analogues could be a safe and more effective combinatory strategy. A critical downside to chloroquine derivatives is the lack of in vivo biomarkers for target engagement. Our results emphasize that ULK1/2 inhibition via SBP-1750 causes a robust decrease in ATG13 which could act as a potent biomarker in future pre-clinical and clinical studies.

Our mechanistic studies show that adaptations to autophagy inhibition led to the most robust sensitivity to pyrimidine analogues, even more so than combining the two drugs in treatment naïve cells, suggest that treating with an autophagy inhibitor prior to a pyrimidine analogue may be the most effective strategy. Modifying the sequence of treatment in this way

would allow autophagy inhibition the necessary time to rewire pyruvate and pyrimidine metabolism to increase pyrimidine salvage. Subsequent treatment with pyrimidine analogues could then be more effective as uptake is increased. Moreover, additional targeting of the pancreas TME that provides pyrimidines could enhance efficacy of this combinatory strategy. We propose that pre-clinical and eventually clinical testing of autophagy inhibition in combination with pyrimidine analogues could improve pancreatic cancer patient outcomes.

ACKNOWLEDGMENTS

This work was supported by an NIH grant R00CA245187 (C.G.T), NIH grant P01CA265762 (R.J.S., A.M.L., D.D.E, H.T.), NIH grant R01CA234245 (C.M.M), NIH grant R35CA220538 (R.J.S.), NIH grant P01CA120964 (R.J.S.), a Pew-Stewart Scholar award 00036071 (C.G.T), a V Foundation scholar award V2023-006 (C.G.T), a Lustgarten Foundation-AACR Career Development Award for Pancreatic Cancer Research in honor of John Robert Lewis 24-20-67-TOWE (C.G.T), Lustgarten Foundation (D.D.E), Conrad Prebys Foundation (D.D.E), Paul M. Angell Family Foundation (D.D.E), Helen McLoraine Developmental Chair (D.D.E), the Salk Alumni Pos-Doctoral Fellowship (S.D.), the T32 CA009370 fellowship (L.R.P., J.E.) the HMMI Hanna H. Gray fellowship GT16776 (L.R.P.), the T32 GM145427 fellowship, (A.K.), the Salk Pioneer fund postdoctoral scholar award (P.M.), and the T32 GM133351 fellowship (A.E.). The targeted metabolomics on nucleotide pools was supported by the Mass Spectrometry Core of the Salk Institute (RRID:SCR_014843) with funding from NIH-NCI CCSG P30 CA014195, NIH-NIA San Diego Nathan Shock Center P30 AG068635, an NIH S10 award for metabolic instrumentation: S10 OD021815, and the Helmsley Center for Genomic Medicine. RNA sequencing experiments were supported by The Razavi Newman Integrative Genomics and Bioinformatics Core Facility of the Salk Institute (RRID:SCR_014842 and SCR_014846) with funding from NIH-NCI CCSG P30 CA014195, NIH-NIA San Diego Nathan Shock Center P30 AG068635, the NIH-NIA Liver Cancer P01 AG073084-04, the Howard and Maryam Newman

Family Foundation and the Helmsley Trust. Sanford Burnham Prebys Medical Discovery Institute core services were supported by NCI Cancer Center support grant P30CA030199. This work was also supported by The Epstein Family Foundation and Pancreatic Action Network Foundation Grant 19 65 COSF (N.D.P.C).

DECLARATION OF INTERESTS

The authors declare no competing interests.

FIGURE LEGENDS

Figure 1. PDA cells that acquire resistance to autophagy inhibition have blocked autophagy

(A) Schematic overview of the process used to make resistant cells.

(B-C) MTT cell viability assay in FC1199 CTL and HCQ-R cells treated with HCQ for 72h (B) and calculated IC50 values (C).

(D-E) MTT cell viability assay in FC1199 CTL and MRT-R cells treated with MRT68921 for 72h (D) and calculated IC50 values (E).

(F-G) Incucyte live cell imaging in FC1199 CTL, HCQ-R or MRT-R cells treated with HCQ or MRT68921 for 3 days.

(H-I) FC1199 CTL, HCQ-R and MRT-R cells transduced with pBabe-mCherry-EGFP-LC3 retrovirus, starved for 24hrs in EBSS, or treated with BafA1 (20nM) for 24hrs. mCherry/eGFP fluorescence was measured by flow cytometry (H) and autophagy induced under EBSS starvation was determined (I).

(J-O) MTT cell viability assay in FC1199 CTL and HCQ-R cells treated with MRT68921 (J-K), DC661 (L-M) or BafA1 (N-O) for 72h and calculated IC50 values.

(P-U) MTT cell viability assay in FC1199 CTL and MRT-R cells treated with HCQ (P-Q), DC661 (R-S) or BafA1 (T-U) for 72h and calculated IC50 values.

Data are represented as a mean ± SEM. Data on panels B, D, F-G, J, L, N, P, R and T show n=3 technical replicates representative of n=3 biological replicates. Data on panels C, E, I, K, M, O, Q, S and U represent n=3 biological replicates. * indicates $p<0.05$, ** $p<0.001$, *** $p<0.0001$, **** $p<0.00001$ determined by two-tailed Student' *t* test (C, E, K, M, O, Q, S and U), two-way ANOVA with Tukey's post hoc test (F-G) and one-way ANOVA with Tukey's post hoc test (I).

Figure 2. PDA cells resistant to autophagy inhibition rewire their metabolism and decrease pyruvate decarboxylation

(A-B) Top metabolism-related GO terms pathway significantly upregulated (A) or downregulated (B) in FC1199 HCQ-R and MRT-R cells compared to CTL and in Atg7 KO cells compared to WT cells.

(C) Heatmaps of metabolite abundances from GC-MS in CTL, HCQ-R and MRT-R cells.

(D) Tracing map for [U-$^{13}C_6$] glucose trace into pyruvate decarboxylation and TCA cycle.

(E-F) Isotopologue abundances calculated as MIDs multiplied by the indicated metabolite abundance from a [U-$^{13}C_6$] glucose trace and GC-MS for pyruvate (E) and citrate (F) in CTL, HCQ-R and MRT-R cells.

(G) Pyruvate decarboxylation measured as M2 Citrate to M3 pyruvate ratio from the [U-$^{13}C_6$] glucose trace in FC1199 CTL, HCQ-R and MRT-R cells.

(H) Pearson correlation of GO macroautophagy gene signature and the reactome regulation of PDH signature in PDA cells determined by single linear regression using data mined from Depmap.

(I-K) Seahorse assay performed in FC1199 CTL, HCQ-R and MRT-R cells (I) with calculated basal (J) and maximal (K) respiration rates displayed as the fold change relative to CTL.

Data are represented as a mean ± SEM. Data on panels C, I-K represent n=3-6 biological replicates. Data on panels E-G are representative of n=3 technical replicates. * indicates $p<0.05$, ** $p<0.001$, *** $p<0.0001$, **** $p<0.00001$, determined by two-tailed Student' *t* test (E-G) and one-way ANOVA with Tukey's post hoc test (I-K).

Figure 3. PDA cells resistant to autophagy inhibition undergo anaplerosis to limit TCA dysfunctions

(A) Tracing map for [U-$^{13}C_6$] glucose trace into pyruvate decarboxylation via PDH and TCA cycle.

(B-D) Fumarate normalized abundance (B) MID (C), and M3 fumarate/M3 pyruvate ratio (D) indicative of pyruvate decarboxylation via PDH in FC1199 CTL and HCQ-R following a [U-$^{13}C_6$] glucose trace and GC-MS.

(E-G) Fumarate normalized abundance (E) MID (F), and M3 fumarate/M3 pyruvate ratio (G) indicative of pyruvate decarboxylation via PDH in FC1199 CTL and MRT-R following a [U-$^{13}C_6$] glucose trace and GC-MS.

(H-J) Malate normalized abundance (H) MID (I), and M3 malate/M3 pyruvate ratio (J) indicative of pyruvate decarboxylation via PDH in FC1199 CTL and HCQ-R following a [U-$^{13}C_6$] glucose trace and GC-MS.

(K-M) Malate normalized abundance (K) MID (L), and M3 malate/M3 pyruvate ratio (M) indicative of pyruvate decarboxylation via PDH in FC1199 CTL and MRT-R following a [U-$^{13}C_6$] glucose trace and GC-MS.

(N-P) Aspartate normalized abundance (N) MID (O), and M3 aspartate/M3 pyruvate ratio (P) indicative of pyruvate decarboxylation via PDH in FC1199 CTL and HCQ-R following a [U-$^{13}C_6$] glucose trace and GC-MS.

(Q-S) Aspartate normalized abundance (Q) MID (R), and M3 aspartate/M3 pyruvate ratio (S) indicative of pyruvate decarboxylation via PDH in FC1199 CTL and MRT-R following a [U-$^{13}C_6$] glucose trace and GC-MS.

(T) Tracing map for [3-$^{13}C_1$] glucose trace into pyruvate decarboxylation via PDH.

(U-V) Pyruvate decarboxylation via PDH measured as M1 aspartate/M1 pyruvate ratio (U) and M1 malate/M1 pyruvate (V) from the [3-$^{13}C_1$] glucose trace and GC-MS in FC1199 CTL and HCQ-R cells.

(W) *Pcx* normalized mRNA expression in FC1199 CTL, HCQ-R and MRT-R cells.

(X) Western blots for PCx and β-Actin in FC1199 CTL, HCQ-R and MRT-R cells. Images are representative of n=3 biological experiments.

Data are represented as a mean ± SEM. Panels B-S and U-V represent n=3 technical replicates. Panel W represents n=3 biological replicates. * indicates $p<0.05$, ** $p<0.001$, *** $p<0.0001$, **** $p<0.00001$, determined by two-tailed Student' *t* test (B, D-E, G-H, J-K, M-N, P-Q, S and U-V), two-way ANOVA with Šidák multiple comparisons test (C, F, I, L, O and R) and one-way ANOVA with Tukey's post hoc test (W).

Figure 4: PDA cells resistant to autophagy inhibition have decreased nucleotide pools and altered pyrimidine metabolism

(A) Overview of the role of pyrimidine synthesis on TPK1 activity and PDH activity, based on findings from Sahu et al. [49]

(B) Normalized *Tpk1* gene expression in FC1199 CTL, HCQ-R and MRT-R cells.

(C) Western blot for TPK1 and α-Tubulin in FC1199 CTL, HCQ-R and MRT-R cells. Images are representative of n=3 biological experiments.

(D) GSEA analysis for pyrimidine metabolism related processes in FC1199 CTL and HCQ-R cells.

(E-F) Heatmaps from LC-MS for free pyrimidine abundances in FC1199 CTL, HCQ-R (E) and MRT-R cells (F).

(G) Schematic overview of the de novo pyrimidine synthesis and pyrimidine salvage pathway.

(H) Western blot for DHODH, CAD, dCK, TK1, SLC29A1 and α-Tubulin in FC1199 CTL, HCQ-R and MRT-R cells. Images are representative of n=3 biological experiments.

(I) Western blot for DHODH, dCK and α-Tubulin in FC1199 g-NT and g-DHODH cells (pool populations).

Data are represented as a mean ± SEM. Panel B represents n=3 biological replicates. Panels E-F represent n=2-11 biological replicates. * indicates $p<0.05$, ** $p<0.001$, *** $p<0.0001$, **** $p<0.00001$, determined by one-way ANOVA with Tukey's post hoc test (B) and two-tailed Student' *t* test (E-F).

Figure 5. PDA cells resistant to autophagy inhibition have increased sensitivity to pyrimidine analogs

(A-B) Log2 fold change between the IC50 of FC1199 HCQ-R and CTL cells (A) or FC1199 MRT-R and CTL cells (B) for the indicated autophagy inhibitors, pyrimidine analogs and other PDAC standard of care compounds determined with MTT cell viability assays. Statistics are determined for each compound on MTT assays in CTL versus HCQ-R or MRT-R cells.

(C) Structure of deoxycytidine compared to gemcitabine and thymidine compared to trifluridine.

(D-G) MTT cell viability assay and the calculated IC50 for FC1199 CTL and HCQ-R cells treated with Gemcitabine (D-E) and FTD/TPI (F-G).

(H) Incucyte live cell imaging in FC1199 CTL and HCQ-R cells treated with gemcitabine (5nM) for 72h.

(I-L) MTT cell viability assay and the calculated IC50 for FC1199 CTL and MRT-R cells treated with Gemcitabine (I-J) and FTD/TPI (K-L).

(M) Incucyte live cell imaging in FC1199 CTL and MRT-R cells treated with FTD/TPI (37.5nM) for 72h.

(N-O) MTT cell viability assay and the calculated IC50 for FC1199 g-NT and g-DHODH treated with gemcitabine for 72h with or without addition of uridine (250μM).

(P) Incucyte live cell imaging in FC1199 CTL and HCQ-R cells treated with gemcitabine (5nM) or vehicle control with or without the addition of deoxycytidine (Dc; 100μM) as indicated for 72h.

(Q) Incucyte live cell imaging in FC1199 CTL and MRT-R cells treated with FTD/TPI (37.5nM) or vehicle control with or without the addition of Thymidine (Thym; 200μM) as indicated for 72h.

(R) MTT cell viability assay in FC1199 g-NT or g-dCK (guide 1 or 2) cells treated with gemcitabine for 72h.

(S-T) Picture (S) and weight (T) of the orthotopic tumors resected from mice injected with FC1245 CTL or HCQ-R cells treated with gemcitabine (5mg/kg, IP, every 3 days) or saline control (n=9-10/group).

(U) Schematic overview of the proposed model by which acquired resistance to autophagy inhibition alters the TCA cycle and pyrimidine metabolism.

Data are represented as a mean ± SEM. Panels A-B, E, G, J, L and O represent n=3 biological replicates. Panels D, F, H-I, K, M-N and P-R represent n=3 technical replicates representative of n=3 biological replicates. * indicates $p<0.05$, ** $p<0.001$, *** $p<0.0001$, **** $p<0.00001$, determined by two-tailed Student' *t* test (A, B, E, G, J, L and O), two-way ANOVA with Tukey's post hoc test (H, M and P-Q) and one-way ANOVA with Tukey's post hoc test (S).

Figure 6: Autophagy inhibitors and pyrimidine analogues have a combinatory effect in PDA

(A-C) Correlation between either (A) autophagy gene signature, (B) *ATG13* expression or (C) *ULK1* expression and gemcitabine sensitivity graphed as area under the curve (AUC) from 72h cell viability assays in hPDOs determined by single linear regression.

(D-F) Incucyte live cell imaging in FC1199 cells treated with MRT and gemcitabine (Gem) as indicated for 3 days and graphed as percent confluence (D) or caspase 3/7 object count/mm^2 normalized to confluence (E) with (F) showing representative phase imaging and cas3/7 object count.

(G-H) Incucyte live cell imaging in FC1199 cells treated with MRT and FTD/TPI as indicated for 3 days and graphed as percent confluence (G) or caspase 3/7 object count/mm^2 normalized to confluence (H) with (F) showing representative phase imaging and cas3/7 object count.

(I-K) Incucyte live cell imaging in FC1199 cells treated with SBP-1750 and gemcitabine (Gem) as indicated for 3 days and graphed as percent confluence (I) or caspase 3/7 object count/mm^2 normalized to confluence (J) with (K) showing representative phase imaging and cas3/7 object count.

(L-M) Incucyte live cell imaging in FC1199 cells treated with SBP-1750 and FTD/TPI as indicated for 3 days and graphed as percent confluence (L) or caspase 3/7 object count/mm^2 normalized to confluence (M) with (K) showing representative phase imaging and cas3/7 object count.

(N-P) Mice injected orthotopically with FC1199 cells and treated with gemcitabine (10mg/kg, IP, every 3 days) and/or SBP-1750 (30mg/kg, PO, daily) or vehicle control with measured body weights (N), Tumor volumes (O) and representative images of tumors (P) from these mice. n = 9-10 per group.

(Q) Western blot for ATG13 and GAPDH in tumors from mice treated with vehicle control (CTL), SBP-1750 or SBP-1750 combined with gemcitabine (Gem + SBP-1750).

Data are represented as a mean ± SEM. Data on panels D-E, G-H, I-J and L-M represent n=3 technical replicates representative of n=3 biological replicates. * indicates $p<0.05$, ** $p<0.001$, *** $p <0.0001$, **** $p<0.00001$, determined by two-way ANOVA with Tukey's post hoc test (D, G, I, and L) and one-way ANOVA with Tukey's post hoc test (E, H, J, and M-O).

EXPERIMENTAL MODELS AND SUBJECT DETAILS

Cell Lines

All cell lines were maintained at 37°C and 5 % CO_2. FC1199 and FC1245 cells were provided by the Tuveson lab and derived from a PDA tumor from a KPC male and female mouse, respectively. These cells were maintained in Dulbecco's Modified Eagle Medium (DMEM; Thermo Fisher

Scientific) with 10 % fetal bovine serum (FBS; Omega Scientific Inc.) and 1% Penicillin-Streptomycin (Pen/Strep; Thermo Fisher Scientific). Kras (G12D) and Trp53 (R172H) mutations in these cells were confirmed via automated genotyping services provided by Transnetyx. MIA PaCa-2 cells were provided from the Engle lab and kept in Roswell Park Memorial Institute medium (RPMI 1640; Thermo Fisher Scientific) with 10 % FBS (Omega Scientific Inc.) and 1% Pen/Strep (Thermo Fisher Scientific). MIA PaCa-2 cells were validated by STR profiling (ATCC). All cell lines were periodically monitored for mycoplasma contamination with the MycoAlert Mycoplasma Detection Kit (Lonza). Generation of FC1199, FC145 and MIA PaCa-2 HCQ-R ad MRT-R cell lines: The IC50 for HCQ (Sigma-Aldrich) or MRT68921 (MedChemExpress) was determined for each cell line using an MTT cell viability assay. Each cell line was treated with the IC50 for several weeks until little cell death was observed. A new IC50 was then determined, and cells were cultured with this new drug dose for several weeks. This process was repeated until cells reached a 5-10-fold resistance compared to CTL drug naïve cells kept in culture in parallel. Once this level of resistance was reached, the cells were kept in culture with drug in the media.

Animal Studies

10–12-week-old C57BL/6J male mice were purchased from The Jackson Laboratory. Mice were housed in filter-topped cages at room temperature (21˚C) in the same room with a 12-hour light: dark cycle. They were fed a standard diet and had access to water ad libitum. 10–12-week-old male mice and 10-week-old female mice were used for FC1199 and FC1245 tumor implantation experiments, respectively. Mice were randomized onto treatment arms and all experimental protocols were approved and performed according to the Institutional Animal Care and Use Committee (IACUC) of the Salk Institute for Biological Studies.

METHOD DETAILS

MTT cell viability assay

PDA cells were plated in 96 well plates (1500-3000 cells per well) or 384 clear well plates (250-500 cells per well). The next day, cells were treated with different doses of the drug of interest in triplicate either manually or with the D300e digital dispenser (Tecan). After 72h, cell viability was measured using MTT assays (R&D Systems) according to the manufacturer's protocol. The Infinite 200 pro M Plex microplate reader (Tecan) was used to measure the absorbance of all wells (including the blanks containing medium only) at 565nM for 180 seconds following a 2min shaking period. The IC50 values were calculated using Graph Pad Prism 10.1.1 (Graph Pad Software Inc).

Incucyte live cell imaging

Live cell imaging was performed with the Incucyte S3 (Sartorius) at 10X magnification. FC1199, FC1245 (1,500-10,000 cells per well) and MIA PaCa-2 CTL cells (5,000-10,000 cells per well) were seeded in 96 well plates. CTL and resistant lines were plated to have equal confluency at the time of dosing. The plates were then placed in the incucyte for 72h, with pictures taken every 4 hours. Cell confluency was determined using the Incucyte S3 software (Sartorius). The CellEvent Caspase 3/7 green reagent (Thermo Fisher Scientific) was used at a 1:1000 concentration to measure caspase 3/7 activity. The reagent was added at the same time as the drugs and green events were counted (optimized for each cell type) and reported relative to cell confluency.

Clonogenic assay

500 cells were plated into 6 well plates. The next day, the media was removed and replaced with media containing drugs of interest or vehicle control. After 72 hours, the media was replaced with drug-free full media for another 5-10 days. Cells were then washed fixed and stained with crystal violet (Sigma-Aldrich).

Measurement of Autophagic Flux by Ratiometric Flow Cytometry

FC1199 CTL, HCQ-R and MRT-R cells were transfected with pBabe-mCherry-EGFP-LC3, kindly gifted by Jayanta Debnath, and used for flow cytometric analysis. Cells were either (1) kept in normal media, (2) changed to EBSS starvation media (Sigma-Aldrich) for 24 hours, or (3) treated with the lysosomal inhibitor BafA1 (20 nM; Sigma-Aldrich) for 24 hours. Flow cytometry was performed with the BD FACS Aria Fusion flow cytometer using 488 and 561nM lasers for green and red fluorophore excitation, respectively. The appropriate side/forward scatter profile was used to exclude non-viable cells. Cells undergoing autophagy are defined based on their mCherry/GFP fluorescence ratio. The gate to define cells undergoing autophagy was set based on cells treated with BafA1 such that 5% of bafilomycin A1-treated cells were included in the gate.

RNA isolation and RNA sequencing

Total RNA was extracted from cells using the RNeasy Plus mini kit (Qiagen) according to the manufacturer's recommendations. RNA concentration was assessed by Qubit Flex Fluorometer (Thermo Fisher Scientific, CA, USA). RNA integrity number was verified with Agilent 2200 TapeStation system (Agilent Technologies, Amsterdam, Netherlands). RNA-seq libraries (cDNA libraries from polyA mRNA) and sequencing were performed at The Razavi Newman Integrative Genomics and Bioinformatics Core Facility of the Salk Institute (RRID:SCR_014842 and SCR_014846). Libraries were prepared by using Illumina's TruSeq RNA library Preparation kit according to manufacturer's instructions (Illumina, San Diego, CA, USA). Libraries were pooled and sequenced using either the Illumina NovaSeq 6000 or NovaSeq X Plus (Illumina, San Diego, CA, USA) with 50-bp paired-end read chemistry. Raw basecalls were demultiplexed to FastQ files using BCL2FastQ v v2.20.0.422 (Illumina, San Diego, CA, USA) and quality assessed using FastQC v0.11.8 (Babraham Bioinformatics, Cambridge, UK).

Metabolite extraction and GC-MS analysis

At the conclusion of the tracer experiment, media was aspirated from all wells. Cells were rinsed on ice with 0.9% saline solution and lysed with 500µl of ice-cold methanol. After 1 min, 100 µl of water containing norvaline (1 µg/ml) was added to each sample and vortexed for 5 min and 50uL was plated on a 96 well plate aside for protein concentration assessment. The 450uL remaining of the lysates were centrifuged at 21,130*g* for 10 min at 4°C. The supernatant was transferred in a microvial (Thermo Fisher Scientific) before being evaporated with a speed-vacuum at 4°C. Dried polar metabolites were processed for gas chromatography–mass spectrometry (GC-MS) as previously described by Cordes and Metallo[81]. Briefly, polar metabolites were derivatized using a Gerstel MultiPur-pose Sampler (MPS 2XL). Methoxime–tert-butyldimethylchlorosi-lane (tBDMS) derivatives were formed by addition of 15 µl of 2%(w/v) methoxylamine hydrochloride (MP Biomedicals, Solon,OH) in pyridine and incubated at 45°C for 60 min. Samples were then silylated by addition of 15 µl of N-tert-butyldimethylsily-N-methyltrifluoroacetamide (MTBSTFA) with 1% tBDMS (RegisTechnologies, Morton Grove, IL) and incubated at 45°C for 30min. Derivatized samples were analyzed using gas GC–MS on a DB-35MS column (30 m × 0.25 mm internal diameter × 0.25 µm, Agilent J&W Scientific) installed in an Agilent 7890A gas chromatograph coupled to an Agilent 5975C mass spectrometer. Samples were injected at an initial oven temperature of 100 °C, held for 1 min, ramped at 3.5 °C/min up to 255°C, then at 15 °C/min up to 320 °C, and held for 3 min. Electron impact ionization was used, and the instrument scanned over the *m/z* range of 100–650.Metabolite quantification and isotopomer distribution analysis were performed using in-house MATLAB scripts, including correction for natural isotope abundance.

High-resolution LC-MS/MS of polar metabolites

Polar metabolites were extracted from confluent six-well plates after growing in DMEM + 10% FBS + 1% penicillin streptomycin for 48 hours. At the conclusion of the experiment, media was aspirated, and the cells were rinsed with saline solution. Cells were lysed with 500 µl of ice-cold

methanol and 200ul of water spiked with norvaline (1 µg/ml) and scraped into Eppendorf tubes. The tubes were vortexed for 5 min and centrifuged at 21,230g at 4°C for 5 min. Polar phase was dried under air, and the pellet was resuspended in 50 µl of acetonitrile and loaded onto LC-MS/MS as previously described[82]. Briefly, samples were loaded on to a Q Exactive orbitrap mass spectrometer with a Vanquish Flex Binary UHPLC system (Thermo Fisher Scientific) that was used with an iHILIC-(P) Classic, 150 by 2.1 mm, 5-µm particle,200 Å (Hilicon) column at 45°C. Five microliters of sample were injected. Chromatography was performed using a gradient of 20 mM ammonium carbonate, adjusted to pH 9.4 with 0.1% ammoniumhydroxide (25%) solution (mobile phase A) and 100% acetonitrile (mobile phase B), both at a flow rate of 0.2 ml/min. The LC gradient ran linearly from 80 to 20% B from 2 to 17 min and then from 20 to80% B from 17 to 18 min and then held at 80% B from 18 to 25 min.

Targeted metabolomics for nucleotide pools

Cell pellets were extracted with the addition of 500 µL of chilled 80% methanol and 10 µL each of the internal standards' glutamic acid-d5 and adenosine triphosphate-13C10, followed by cycles of 2 min sonication in an ice bath and 30 sec vortexing to resuspend cell pellets. Samples were next placed on dry ice for 30 min prior to centrifugation (14,000 x g, 4 C, 10 min). The supernatant was transferred to a new tube and dried under nitrogen gas. Samples were reconstituted in 100 µL of 20% methanol, vortexed 30 sec, and transferred to HPLC vials prior to LC-MS analysis for nucleotides. The remaining cell pellet underwent total protein concentration analysis on a Synergy H1 Hybrid reader (BioTek Instruments, Inc., Winooski, VT, USA). Nucleotides were analyzed on an Ultimate 3000 UHPLC system (Thermo Fisher, Waltham, MA, USA) coupled to a TSQ Quantiva mass spectrometer (Thermo Fisher) with separation performed on a Waters 4.6 x 100 mm, 3.5 µm XBridge Amide HILIC column (Waters Corporation, Milford, MA, USA). LC solvents included mobile phase A consisting of 95:5 water:acetonitrile, 20 mM ammonium hydroxide, 20 mM ammonium acetate, and mobile phase B consisting of 100 % acetonitrile. A gradient was

used with a flow rate of 0.4 mL/min. Injection volume was 10 µL, the column oven temperature was set to 25 C. MS analyses were performed using electrospray ionization in negative ionization mode. Spray voltage was -3.5kV, ion transfer tube temperature of 325 C, and vaporizer temperature of 275 C. Multiple reaction monitoring (MRM) was performed. Skyline software v. 24.1.0.199[83] was used to measure peak areas. Peak areas were normalized using internal standards and protein concentration.

Seahorse assay

10,000 cells were plated in 96-well plates (XFe96 plates, Agilent) in technical replicates of 6-8 and incubated at 37°C overnight. The next day, the medium was changed to XF Assay Medium (Agilent) containing 10 mM glucose, 1 mM pyruvate, and 2 mM glutamine and the cells were incubated at 37°C for one hour in a non-CO_2 incubator. The Seahorse XF mitochondrial stress test (Agilent) was performed according to manufacturer's instructions and oxygen consumption rates (OCR) were measured with a Seahorse XFe96 extracellular flux analyzer (Agilent). Briefly, basal OCR was measured prior to the addition of oligomycin (0.5µM), followed by 3 more OCR measurements and then carbonilcyanide p-triflouromethoxyphenylhydrazone (FCCP) (2µM) was added. Three more OCR measurements were taken before Rotenone/Antimycin-A (0.5µM) was added followed by three final OCR measurements. All data was analyzed in Wave software and normalized to confluency (assessed by a scan-on-demand in the Incucyte performed immediately after the mito stress test). The parameter values were calculated in Wave as follows: Basal respiration – Last rate measurement before the first injection subtract the non-mitochondrial respiration rate (minimum rate measurement after Rotenone/Antimycin-A injection), spare respiratory capacity – maximal respiration (maximum rate measurement after FCCCP injection subtract the non-mitochondrial respiration rate) subtract basal respiration.

Western Blotting

Whole cell lysate samples were washed with cold PBS and harvested on ice with RIPA buffer and 1X of protease inhibitor cocktail (Roche) added just before use. Lysates were sonicated before being spined down at 20 000xg for 15min at 4C. The pellet was discarded, and supernatant was kept. Protein concentration was determined with a Bradford assay and was measured relative to a bovine serum albumin (BSA) standard curve. Western blotting was performed using standard methods including protein separation on SDS-PAGE 1.5mm mini gels in running buffer at 100V for 2hrs, followed by transfer to PVDF membranes in transfer buffer using a semi-dry transfer apparatus at 15V for 70 minutes. Membranes were blocked in 5% milk for 1hr at room temperature with gentle rocking, washed twice in 1X TBST, and then incubated overnight at 4°C with gentle rocking in primary antibodies. Membranes were then washed three times in TBST and incubated for 1hr at room temperature with gently rocking in secondary antibodies followed by 3 more TBST washes. Membranes were developed with Immobilon Western chemiluminescent HRP substrate (Sigma-Aldrich) and analyzed on the ChemiDoc imaging system (Bio-Rad). Antibodies are listed in the Key Resources Table. Protein expression was calculated using ImageJ and expressed as a ratio between protein of interest to loading control. Experimental samples were then normalized to controls.

Electroporation with RNPs

The CRISPR/Cas9 system was used to generate DHODH and dCK KO and non-targeting (NT) FC1199 cell lines. For DHODH KO lines, the cells were passaged and maintained in media containing uridine, based on prior studies showing DHODH KO cells are uridine auxotrophs[53,49,54,52,51]. For experimentation using DHODH KO as a model to deplete pyrimidine pools, uridine was removed. Electroporation was performed using the 4D-Nucleofector system (Lonza Bioscience) with the P3 Primary Cell 4D-Nucleofector X Kit S (Lonza Bioscience), following the manufacturer's instructions. sgRNA were obtained from Synthego and reconstituted in TE buffer at 0.5nM/µL. To form RNPs for each condition, 0.5nM of sgRNA was incubated at

room temperature for 10min with 6µg of Cas9 (PNA Bio), previously resuspended in a 20% glycerol buffer at 5µg/ml. Two million FC1199 cells were mixed with the RNP complexes and transferred to a well of a Nucleocuvette Strip. The strip was then electroporated on the Lonza 4D electroporation system with pulse code CZ167 (Cell Type Program MEF, mouse). Knock-out was confirmed by western blot one week post electroporation.

Pharmacotyping in hPDOs and response correlation with gene expression

We used previously published methods and organoids[69]. Briefly, PDAC organoids were plated in 384-well plates at the density of 1,000 cells per well in 20µL media. Drugs were dispensed in each well using the D300e Digital Dispenser (Tecan). 5-days after treatment, cell viability was measured using a luminescent ATP-based assay (CellTiter-Glo, Promega) and Synergy H1 plate reader. To assess hPDO response correlation with gene expression, we performed a Pearson correlation of gemcitabine sensitivity (area under the curve from Tiriac et al.[69], low AUC indicates sensitivity to gemcitabine) and the Autophagy gene signature[84].

Mouse treatments

2000 FC1199 and FC1245 CTL and HCQ-R cells were injected orthotopically in the pancreas of 10-week-old C57BL/6J male mice (Jackson) in 30uL of a 1:1 serum-free DMEM media (Thermo Fisher Scientific) and Matrigel (Corning) mixture. Eight days after the injection, mice received gemcitabine (5mg/kg, IP, every 3 days; McKesson Medical-Surgical Inc.) or saline control (Pfizer). Mice were euthanized 21-22 days after cell injections. For combination treatment experiments, 1000 drug-naïve FC1199 cells were also injected orthotopically in the pancreas of 12-week-old C57BL/6J male mice as described above. The mice received SBP-1750 (30mg/kg, PO, daily) or vehicle control, and gemcitabine (10mg/kg, IP, every 3 days; McKesson Medical-Surgical Inc.) or saline (Pfizer) control. Mice were euthanized 28 days after the orthotopic surgery, and 2-3 hours after the last drug treatment.

Histology

Mice were euthanized and tissues were fixed in 10% neutral buffered formalin (Epredia). All sample preparation and staining procedures were then performed at HistoWiz Inc., using HistoWiz's Standard Operating Procedure, and a fully automated workflow. Samples were processed, embedded in paraffin, and sectioned at 4 μm. Slides were stained by a standard H&E staining protocol (Histowiz, Long Island City NY). The slides were then dried, and film-coverslipped using a TissueTek-Prisma and Coverslipper (Sakura). Whole-slide scanning (40×) was performed on an Aperio AT2 (Leica Biosystems).

Quantification and Statistical Analysis

Statistical analyses and graphs were performed using Graph Pad Prism 10.1.1 (Graph Pad Software Inc). A two-tailed Students t-test was used for comparisons between two groups. For analyses involving more than two groups, either a one-way ANOVA followed by Tukey's post hoc test (for a single variable) or a two-way ANOVA with Tukey's post hoc test (for multiple variables) was performed. For non-normally distributed data, a Mann-Whitney test or a Kruskal-Wallis test were performed for comparisons between two groups and more than two groups with a single variable, respectively. Graphs were made with Graph Pad Prism 10.1.1 (Graph Pad Software Inc). with the error bars representing mean with standard deviation. All group numbers and explanation of significant values are presented within the figure legends. $^{*}p < 0.05$; $^{**}p < 0.01$; $^{***}p < 0.001$; $^{****}p < 0.0001$.

REFERENCES

1. Levy, J.M.M., Towers, C.G., and Thorburn, A. (2017). Targeting autophagy in cancer. Nat Rev Cancer *17*, 528–542. https://doi.org/10.1038/nrc.2017.53.

2. Assi, M., and Kimmelman, A.C. (2023). Impact of context-dependent autophagy states on tumor progression. Nat Cancer *4*, 596–607. https://doi.org/10.1038/s43018-023-00546-7.

3. Debnath, J., Gammoh, N., and Ryan, K.M. (2023). Autophagy and autophagy-related pathways in cancer. Nat Rev Mol Cell Biol *24*, 560–575. https://doi.org/10.1038/s41580-023-00585-z.

4. Jain, V., Singh, M.P., and Amaravadi, R.K. (2023). Recent advances in targeting autophagy in cancer. Trends in Pharmacological Sciences *44*, 290–302. https://doi.org/10.1016/j.tips.2023.02.003.

5. Levine, B., and Kroemer, G. (2019). Biological Functions of Autophagy Genes: A Disease Perspective. Cell *176*, 11–42. https://doi.org/10.1016/j.cell.2018.09.048.

6. Mizushima, N. (2020). The ATG conjugation systems in autophagy. Curr Opin Cell Biol *63*, 1–10. https://doi.org/10.1016/j.ceb.2019.12.001.

7. Yamamoto, H., Zhang, S., and Mizushima, N. (2023). Autophagy genes in biology and disease. Nat Rev Genet *24*, 382–400. https://doi.org/10.1038/s41576-022-00562-w.

8. Guo, J.Y., Chen, H.-Y., Mathew, R., Fan, J., Strohecker, A.M., Karsli-Uzunbas, G., Kamphorst, J.J., Chen, G., Lemons, J.M.S., Karantza, V., et al. (2011). Activated Ras requires autophagy to maintain oxidative metabolism and tumorigenesis. Genes Dev *25*, 460–470. https://doi.org/10.1101/gad.2016311.

9. Yang, S., Wang, X., Contino, G., Liesa, M., Sahin, E., Ying, H., Bause, A., Li, Y., Stommel, J.M., Dell'Antonio, G., et al. (2011). Pancreatic cancers require autophagy for tumor growth. Genes Dev. *25*, 717–729. https://doi.org/10.1101/gad.2016111.

10. Perera, R.M., Stoykova, S., Nicolay, B.N., Ross, K.N., Fitamant, J., Boukhali, M., Lengrand, J., Deshpande, V., Selig, M.K., Ferrone, C.R., et al. (2015). Transcriptional control of the autophagy-lysosome system in pancreatic cancer. Nature *524*, 361–365. https://doi.org/10.1038/nature14587.

11. Degenhardt, K., Mathew, R., Beaudoin, B., Bray, K., Anderson, D., Chen, G., Mukherjee, C., Shi, Y., Gélinas, C., Fan, Y., et al. (2006). Autophagy promotes tumor cell survival and restricts necrosis, inflammation, and tumorigenesis. Cancer Cell *10*, 51–64. https://doi.org/10.1016/j.ccr.2006.06.001.

12. Lock, R., Roy, S., Kenific, C.M., Su, J.S., Salas, E., Ronen, S.M., and Debnath, J. (2011). Autophagy facilitates glycolysis during Ras-mediated oncogenic transformation. Mol Biol Cell *22*, 165–178. https://doi.org/10.1091/mbc.E10-06-0500.

13. Karsli-Uzunbas, G., Guo, J.Y., Price, S., Teng, X., Laddha, S.V., Khor, S., Kalaany, N.Y., Jacks, T., Chan, C.S., Rabinowitz, J.D., et al. (2014). Autophagy is required for glucose homeostasis and lung tumor maintenance. Cancer Discov *4*, 914–927. https://doi.org/10.1158/2159-8290.CD-14-0363.

14. Sousa, C.M., Biancur, D.E., Wang, X., Halbrook, C.J., Sherman, M.H., Zhang, L., Kremer, D., Hwang, R.F., Witkiewicz, A.K., Ying, H., et al. (2016). Pancreatic stellate cells support tumour metabolism through autophagic alanine secretion. Nature *536*, 479–483. https://doi.org/10.1038/nature19084.

15. Ravichandran, M., Hu, J., Cai, C., Ward, N.P., Venida, A., Foakes, C., Kuljanin, M., Yang, A., Hennessey, C.J., Yang, Y., et al. (2022). Coordinated Transcriptional and Catabolic Programs Support Iron-Dependent Adaptation to RAS–MAPK Pathway Inhibition in Pancreatic Cancer. Cancer Discovery *12*, 2198–2219. https://doi.org/10.1158/2159-8290.CD-22-0044.

16. Mukhopadhyay, S., Encarnación-Rosado, J., Lin, E.Y., Sohn, A.S.W., Zhang, H., Mancias, J.D., and Kimmelman, A.C. (2023). Autophagy supports mitochondrial metabolism through the regulation of iron homeostasis in pancreatic cancer. Science Advances *9*, eadf9284. https://doi.org/10.1126/sciadv.adf9284.

17. Kimmelman, A.C., and White, E. (2017). Autophagy and Tumor Metabolism. Cell Metabolism *25*, 1037–1043. https://doi.org/10.1016/j.cmet.2017.04.004.

18. Poillet-Perez, L., and White, E. (2019). Role of tumor and host autophagy in cancer metabolism. Genes Dev. *33*, 610–619. https://doi.org/10.1101/gad.325514.119.

19. Fujiwara, Y., Furuta, A., Kikuchi, H., Aizawa, S., Hatanaka, Y., Konya, C., Uchida, K., Yoshimura, A., Tamai, Y., Wada, K., et al. (2013). Discovery of a novel type of autophagy targeting RNA. Autophagy *9*, 403–409. https://doi.org/10.4161/auto.23002.

20. Fujiwara, Y., Kikuchi, H., Aizawa, S., Furuta, A., Hatanaka, Y., Konya, C., Uchida, K., Wada, K., and Kabuta, T. (2013). Direct uptake and degradation of DNA by lysosomes. Autophagy *9*, 1167–1171. https://doi.org/10.4161/auto.24880.

21. Guo, J.Y., Teng, X., Laddha, S.V., Ma, S., Van Nostrand, S.C., Yang, Y., Khor, S., Chan, C.S., Rabinowitz, J.D., and White, E. (2016). Autophagy provides metabolic substrates to maintain energy charge and nucleotide pools in Ras-driven lung cancer cells. Genes Dev *30*, 1704–1717. https://doi.org/10.1101/gad.283416.116.

22. Elliott, I.A., Dann, A.M., Xu, S., Kim, S.S., Abt, E.R., Kim, W., Poddar, S., Moore, A., Zhou, L., Williams, J.L., et al. (2019). Lysosome inhibition sensitizes pancreatic cancer to replication stress by aspartate depletion. Proceedings of the National Academy of Sciences *116*, 6842–6847. https://doi.org/10.1073/pnas.1812410116.

23. Santana-Codina, N., Roeth, A.A., Zhang, Y., Yang, A., Mashadova, O., Asara, J.M., Wang, X., Bronson, R.T., Lyssiotis, C.A., Ying, H., et al. (2018). Oncogenic KRAS supports pancreatic cancer through regulation of nucleotide synthesis. Nat Commun *9*, 4945. https://doi.org/10.1038/s41467-018-07472-8.

24. Yang, A., Rajeshkumar, N.V., Wang, X., Yabuuchi, S., Alexander, B.M., Chu, G.C., Hoff, D.D.V., Maitra, A., and Kimmelman, A.C. (2014). Autophagy Is Critical for Pancreatic Tumor Growth and Progression in Tumors with p53 Alterations. Cancer Discov *4*, 905–913. https://doi.org/10.1158/2159-8290.CD-14-0362.

25. Yang, A., Herter-Sprie, G., Zhang, H., Lin, E.Y., Biancur, D., Wang, X., Deng, J., Hai, J., Yang, S., Wong, K.-K., et al. (2018). Autophagy sustains pancreatic cancer growth through both cell autonomous and non-autonomous mechanisms. Cancer Discov *8*, 276–287. https://doi.org/10.1158/2159-8290.CD-17-0952.

26. Petherick, K.J., Conway, O.J.L., Mpamhanga, C., Osborne, S.A., Kamal, A., Saxty, B., and Ganley, I.G. (2015). Pharmacological Inhibition of ULK1 Kinase Blocks Mammalian Target of

Rapamycin (mTOR)-dependent Autophagy. J Biol Chem *290*, 11376–11383. https://doi.org/10.1074/jbc.C114.627778.

27. Ren, H., Bakas, N.A., Vamos, M., Chaikuad, A., Limpert, A.S., Wimer, C.D., Brun, S.N., Lambert, L.J., Tautz, L., Celeridad, M., et al. (2020). Design, Synthesis, and Characterization of an Orally Active Dual-Specific ULK1/2 Autophagy Inhibitor that Synergizes with the PARP Inhibitor Olaparib for the Treatment of Triple-Negative Breast Cancer. J. Med. Chem. *63*, 14609–14625. https://doi.org/10.1021/acs.jmedchem.0c00873.

28. Zachari, M., Longo, M., and Ganley, I.G. (2020). Aberrant autophagosome formation occurs upon small molecule inhibition of ULK1 kinase activity. Life Sci Alliance *3*, e202000815. https://doi.org/10.26508/lsa.202000815.

29. Brun, S.N., Sancar, G., Lumibao, J., Limpert, A.S., Ren, H., Ianniciello, A., Tiriac, H., Downes, M., Engle, D.D., Evans, R.M., et al. (2021). The autophagy initiating kinase ULK1 is required for pancreatic cancer cell growth and survival. Preprint at bioRxiv, https://doi.org/10.1101/2021.05.15.444304 https://doi.org/10.1101/2021.05.15.444304.

30. Ghazi, P.C., O'Toole, K.T., Srinivas Boggaram, S., Scherzer, M.T., Silvis, M.R., Zhang, Y., Bogdan, M., Smith, B.D., Lozano, G., Flynn, D.L., et al. (2024). Inhibition of ULK1/2 and KRASG12C controls tumor growth in preclinical models of lung cancer. eLife *13*, RP96992. https://doi.org/10.7554/eLife.96992.

31. Layng, F.I.A.L., Ren, H., Bakas, N.A., Panickar, D.R., Lambert, L.J., Celeridad, M., Wu, J., Backer, L.D., Chandrachud, P., Limpert, A.S., et al. (2025). Synthesis and Characterization of ULK1/2 Kinase Inhibitors that Inhibit Autophagy and Upregulate Expression of Major Histocompatibility Complex I for the Treatment of Non-Small Cell Lung Cancer. Preprint at bioRxiv, https://doi.org/10.1101/2025.09.05.674519 https://doi.org/10.1101/2025.09.05.674519.

32. Qiao, Y., Choi, J.E., Tien, J.C., Simko, S.A., Rajendiran, T., Vo, J.N., Delekta, A.D., Wang, L., Xiao, L., Hodge, N.B., et al. (2021). Autophagy inhibition by targeting PIKfyve potentiates response to immune checkpoint blockade in prostate cancer. Nat Cancer *2*, 978–993. https://doi.org/10.1038/s43018-021-00237-1.

33. DeLiberty, J.M., Roach, M.K., Stalnecker, C.A., Robb, R., Schechter, E.G., Pieper, N.L., Taylor, K.E., Pita, L.M., Yang, R., Bang, S., et al. (2025). Concurrent Inhibition of the RAS-MAPK Pathway and PIKfyve Is a Therapeutic Strategy for Pancreatic Cancer. Cancer Research *85*, 1479–1495. https://doi.org/10.1158/0008-5472.CAN-24-1757.

34. Cheng, C., Hu, J., Mannan, R., He, T., Bhattacharyya, R., Magnuson, B., Wisniewski, J.P., Peters, S., Karim, S.A., MacLean, D.J., et al. (2025). Targeting PIKfyve-driven lipid metabolism in pancreatic cancer. Nature, 1–9. https://doi.org/10.1038/s41586-025-08917-z.

35. Towers, C.G., and Thorburn, A. (2016). Therapeutic Targeting of Autophagy. EBioMedicine *14*, 15–23. https://doi.org/10.1016/j.ebiom.2016.10.034.

36. Karasic, T.B., O'Hara, M.H., Loaiza-Bonilla, A., Reiss, K.A., Teitelbaum, U.R., Borazanci, E., De Jesus-Acosta, A., Redlinger, C., Burrell, J.A., Laheru, D.A., et al. (2019). Effect of Gemcitabine and nab-Paclitaxel With or Without Hydroxychloroquine on Patients With

Advanced Pancreatic Cancer. JAMA Oncol *5*, 993–998. https://doi.org/10.1001/jamaoncol.2019.0684.

37. Towers, C.G., Fitzwalter, B.E., Regan, D., Goodspeed, A., Morgan, M.J., Liu, C.-W., Gustafson, D.L., and Thorburn, A. (2019). Cancer Cells Upregulate NRF2 Signaling to Adapt to Autophagy Inhibition. Dev Cell *50*, 690-703.e6. https://doi.org/10.1016/j.devcel.2019.07.010.

38. Towers, C.G., Wodetzki, D.K., Thorburn, J., Smith, K.R., Caino, M.C., and Thorburn, A. (2021). Mitochondrial-derived vesicles compensate for loss of LC3-mediated mitophagy. Dev Cell *56*, 2029-2042.e5. https://doi.org/10.1016/j.devcel.2021.06.003.

39. Bryant, K.L., Stalnecker, C.A., Zeitouni, D., Klomp, J.E., Peng, S., Tikunov, A.P., Gunda, V., Pierobon, M., Waters, A.M., George, S.D., et al. (2019). Combination of ERK and autophagy inhibition as a treatment approach for pancreatic cancer. Nat Med *25*, 628–640. https://doi.org/10.1038/s41591-019-0368-8.

40. Kinsey, C.G., Camolotto, S.A., Boespflug, A.M., Gullien, K.P., Foth, M., Truong, A., Schuman, S.S., Shea, J.E., Seipp, M.T., Yap, J.T., et al. (2019). Protective autophagy elicited by RAF→MEK→ERK inhibition suggests a treatment strategy for RAS-driven cancers. Nat Med *25*, 620–627. https://doi.org/10.1038/s41591-019-0367-9.

41. Stalnecker, C.A., Grover, K.R., Edwards, A.C., Coleman, M.F., Yang, R., DeLiberty, J.M., Papke, B., Goodwin, C.M., Pierobon, M., Petricoin, E.F., et al. (2022). Concurrent inhibition of IGF1R and ERK increases pancreatic cancer sensitivity to autophagy inhibitors. Cancer Res *82*, 586–598. https://doi.org/10.1158/0008-5472.CAN-21-1443.

42. Jain, V., Harper, S.L., Versace, A.M., Fingerman, D., Brown, G.S., Bhardwaj, M., Crissey, M.A.S., Goldman, A.R., Ruthel, G., Liu, Q., et al. (2023). Targeting UGCG overcomes resistance to lysosomal autophagy inhibition. Cancer Discov *13*, 454–473. https://doi.org/10.1158/2159-8290.CD-22-0535.

43. Su, H., Yang, F., Fu, R., Li, X., French, R., Mose, E., Pu, X., Trinh, B., Kumar, A., Liu, J., et al. (2021). Cancer cells escape autophagy inhibition via NRF2-induced macropinocytosis. Cancer Cell *39*, 678-693.e11. https://doi.org/10.1016/j.ccell.2021.02.016.

44. Kimura, S., Noda, T., and Yoshimori, T. (2007). Dissection of the autophagosome maturation process by a novel reporter protein, tandem fluorescent-tagged LC3. Autophagy *3*, 452–460. https://doi.org/10.4161/auto.4451.

45. Zhou, C., Zhong, W., Zhou, J., Sheng, F., Fang, Z., Wei, Y., Chen, Y., Deng, X., Xia, B., and Lin, J. (2012). Monitoring autophagic flux by an improved tandem fluorescent-tagged LC3 (mTagRFP-mWasabi-LC3) reveals that high-dose rapamycin impairs autophagic flux in cancer cells. Autophagy *8*, 1215–1226. https://doi.org/10.4161/auto.20284.

46. DepMap: The Cancer Dependency Map Project at Broad Institute https://depmap.org/portal/.

47. Arafeh, R., Shibue, T., Dempster, J.M., Hahn, W.C., and Vazquez, F. (2025). The present and future of the Cancer Dependency Map. Nat Rev Cancer *25*, 59–73. https://doi.org/10.1038/s41568-024-00763-x.

48. Buescher, J.M., Antoniewicz, M.R., Boros, L.G., Burgess, S.C., Brunengraber, H., Clish, C.B., DeBerardinis, R.J., Feron, O., Frezza, C., Ghesquiere, B., et al. (2015). A roadmap for interpreting 13C metabolite labeling patterns from cells. Curr Opin Biotechnol *34*, 189–201. https://doi.org/10.1016/j.copbio.2015.02.003.

49. Sahu, U., Villa, E., Reczek, C.R., Zhao, Z., O'Hara, B.P., Torno, M.D., Mishra, R., Shannon, W.D., Asara, J.M., Gao, P., et al. (2024). Pyrimidines maintain mitochondrial pyruvate oxidation to support de novo lipogenesis. Science *383*, 1484–1492. https://doi.org/10.1126/science.adh2771.

50. Chandel, N.S. (2021). Nucleotide Metabolism. Cold Spring Harb Perspect Biol *13*, a040592. https://doi.org/10.1101/cshperspect.a040592.

51. Ali, E.S., and Ben-Sahra, I. (2023). Regulation of nucleotide metabolism in cancers and immune disorders. Trends in Cell Biology *33*, 950–966. https://doi.org/10.1016/j.tcb.2023.03.003.

52. Mullen, N.J., and Singh, P.K. (2023). Nucleotide metabolism: a pan-cancer metabolic dependency. Nat Rev Cancer *23*, 275–294. https://doi.org/10.1038/s41568-023-00557-7.

53. Bajzikova, M., Kovarova, J., Coelho, A.R., Boukalova, S., Oh, S., Rohlenova, K., Svec, D., Hubackova, S., Endaya, B., Judasova, K., et al. (2019). Reactivation of Dihydroorotate Dehydrogenase-Driven Pyrimidine Biosynthesis Restores Tumor Growth of Respiration-Deficient Cancer Cells. Cell Metab *29*, 399-416.e10. https://doi.org/10.1016/j.cmet.2018.10.014.

54. Brisudova, P., Stojanovic, D., Novak, J., Nahacka, Z., Oliveira, G.L., Vanatko, O., Dvorakova, S., Endaya, B., Truksa, J., Kubiskova, M., et al. (2025). Functional mitochondrial respiration is essential for glioblastoma tumour growth. Oncogene *44*, 2588–2603. https://doi.org/10.1038/s41388-025-03429-6.

55. Peters, G.J., Braakhuis, B.J., de Bruijn, E.A., Laurensse, E.J., van Walsum, M., and Pinedo, H.M. (1989). Enhanced therapeutic efficacy of 5'deoxy-5-fluorouridine in 5-fluorouracil resistant head and neck tumours in relation to 5-fluorouracil metabolising enzymes. Br J Cancer *59*, 327–334. https://doi.org/10.1038/bjc.1989.65.

56. Ichikawa, W., Uetake, H., Shirota, Y., Yamada, H., Takahashi, T., Nihei, Z., Sugihara, K., Sasaki, Y., and Hirayama, R. (2003). Both gene expression for orotate phosphoribosyltransferase and its ratio to dihydropyrimidine dehydrogenase influence outcome following fluoropyrimidine-based chemotherapy for metastatic colorectal cancer. Br J Cancer *89*, 1486–1492. https://doi.org/10.1038/sj.bjc.6601335.

57. Shitara, K., Doi, T., Dvorkin, M., Mansoor, W., Arkenau, H.-T., Prokharau, A., Alsina, M., Ghidini, M., Faustino, C., Gorbunova, V., et al. (2018). Trifluridine/tipiracil versus placebo in patients with heavily pretreated metastatic gastric cancer (TAGS): a randomised, double-blind, placebo-controlled, phase 3 trial. The Lancet Oncology *19*, 1437–1448. https://doi.org/10.1016/S1470-2045(18)30739-3.

58. Prager, G.W., Taieb, J., Fakih, M., Ciardiello, F., Cutsem, E.V., Elez, E., Cruz, F.M., Wyrwicz, L., Stroyakovskiy, D., Pápai, Z., et al. (2023). Trifluridine–Tipiracil and Bevacizumab in

Refractory Metastatic Colorectal Cancer. New England Journal of Medicine *388*, 1657–1667. https://doi.org/10.1056/NEJMoa2214963.

59. Jensen, L.B., Yilmaz, M., Nordsmark, M., Möller, S., Elle, I.C., Ladekarl, M., Qvortrup, C., and Pfeiffer, P. (2024). TRIFLURIDINE/TIPIRACIL (FTD/TPI) with or without bevacizumab in previously treated patients with esophago-gastric adenocarcinoma, a randomised phase III trial. eClinicalMedicine *70*. https://doi.org/10.1016/j.eclinm.2024.102521.

60. de Sousa Cavalcante, L., and Monteiro, G. (2014). Gemcitabine: Metabolism and molecular mechanisms of action, sensitivity and chemoresistance in pancreatic cancer. European Journal of Pharmacology *741*, 8–16. https://doi.org/10.1016/j.ejphar.2014.07.041.

61. Beutel, A.K., and Halbrook, C.J. (2023). Barriers and opportunities for gemcitabine in pancreatic cancer therapy. American Journal of Physiology-Cell Physiology *324*, C540–C552. https://doi.org/10.1152/ajpcell.00331.2022.

62. Kunos, C.A., Chiu, S., Pink, J., and Kinsella, T.J. (2009). Modulating radiation resistance by inhibiting ribonucleotide reductase in cancers with virally or mutationally silenced p53 protein. Radiat Res *172*, 666–676. https://doi.org/10.1667/RR1858.1.

63. Stegmann, A.P., Honders, W.H., Willemze, R., Ruiz van Haperen, V.W., and Landegent, J.E. (1995). Transfection of wild-type deoxycytidine kinase (dck) cDNA into an AraC- and DAC-resistant rat leukemic cell line of clonal origin fully restores drug sensitivity. Blood *85*, 1188–1194.

64. Manome, Y., Wen, P.Y., Dong, Y., Tanaka, T., Mitchell, B.S., Kufe, D.W., and Fine, H.A. (1996). Viral vector transduction of the human deoxycytidine kinase cDNA sensitizes glioma cells to the cytotoxic effects of cytosine arabinoside in vitro and in vivo. Nat Med *2*, 567–573. https://doi.org/10.1038/nm0596-567.

65. van der Wilt, C.L., Kroep, J.R., Bergman, A.M., Loves, W.J., Alvarez, E., Talianidis, I., Eriksson, S., van Groeningen, C.J., Pinedo, H.M., and Peters, G.J. (2000). The role of deoxycytidine kinase in gemcitabine cytotoxicity. Adv Exp Med Biol *486*, 287–290. https://doi.org/10.1007/0-306-46843-3_56.

66. Maréchal, R., Bachet, J., Mackey, J.R., Dalban, C., Demetter, P., Graham, K., Couvelard, A., Svrcek, M., Bardier–Dupas, A., Hammel, P., et al. (2012). Levels of Gemcitabine Transport and Metabolism Proteins Predict Survival Times of Patients Treated With Gemcitabine for Pancreatic Adenocarcinoma. Gastroenterology *143*, 664-674.e6. https://doi.org/10.1053/j.gastro.2012.06.006.

67. Edahiro, K., Iimori, M., Kobunai, T., Morikawa-Ichinose, T., Miura, D., Kataoka, Y., Niimi, S., Wakasa, T., Saeki, H., Oki, E., et al. (2018). Thymidine Kinase 1 Loss Confers Trifluridine Resistance without Affecting 5-Fluorouracil Metabolism and Cytotoxicity. Molecular Cancer Research *16*, 1483–1490. https://doi.org/10.1158/1541-7786.MCR-17-0686.

68. Kataoka, Y., Iimori, M., Niimi, S., Tsukihara, H., Wakasa, T., Saeki, H., Oki, E., Maehara, Y., and Kitao, H. (2019). Cytotoxicity of trifluridine correlates with the thymidine kinase 1 expression level. Sci Rep *9*, 7964. https://doi.org/10.1038/s41598-019-44399-6.

69. Tiriac, H., Belleau, P., Engle, D.D., Plenker, D., Deschênes, A., Somerville, T.D.D., Froeling, F.E.M., Burkhart, R.A., Denroche, R.E., Jang, G.-H., et al. (2018). Organoid Profiling Identifies Common Responders to Chemotherapy in Pancreatic Cancer. Cancer Discov *8*, 1112–1129. https://doi.org/10.1158/2159-8290.CD-18-0349.

70. Bordi, M., De Cegli, R., Testa, B., Nixon, R.A., Ballabio, A., and Cecconi, F. (2021). A gene toolbox for monitoring autophagy transcription. Cell Death Dis *12*, 1–7. https://doi.org/10.1038/s41419-021-04121-9.

71. Shaw, R.J., Egan, D.F., Cosford, N., Turk, B., Vamos, M., Panickar, D.R., Chun, M., and Sheffler, D. (2019). ULK1 inhibitors and methods using same. US 10266549-B2.

72. Ren, H., Bakas, N.A., Vamos, M., Chaikuad, A., Limpert, A.S., Wimer, C.D., Brun, S.N., Lambert, L.J., Tautz, L., Celeridad, M., et al. (2020). Design, Synthesis, and Characterization of an Orally Active Dual-Specific ULK1/2 Autophagy Inhibitor that Synergizes with the PARP Inhibitor Olaparib for the Treatment of Triple-Negative Breast Cancer. J Med Chem *63*, 14609–14625. https://doi.org/10.1021/acs.jmedchem.0c00873.

73. Hagan, P.M., Ren, H., Brun, S.N., Layng, F.I.A.L., Panickar, D.R., Lambert, L.J., Celeridad, M., Das, R., Ling, L., Zhang, Y., et al. (2025). ULK1/2 Inhibitors that Degrade ATG13 Effectively Target KRAS-Mutant Cancers. Preprint at bioRxiv, https://doi.org/10.1101/2025.10.14.682402 https://doi.org/10.1101/2025.10.14.682402.

74. Wong, P.-M., Feng, Y., Wang, J., Shi, R., and Jiang, X. (2015). Regulation of autophagy by coordinated action of mTORC1 and protein phosphatase 2A. Nat Commun *6*, 8048. https://doi.org/10.1038/ncomms9048.

75. Wang, H., Lu, J., Kulkarni, S., Zhang, W., Gorka, J.E., Mandel, J.A., Goetzman, E.S., and Prochownik, E.V. (2019). Metabolic and oncogenic adaptations to pyruvate dehydrogenase inactivation in fibroblasts. Journal of Biological Chemistry *294*, 5466–5486. https://doi.org/10.1074/jbc.RA118.005200.

76. Elia, I., Rowe, J.H., Johnson, S., Joshi, S., Notarangelo, G., Kurmi, K., Weiss, S., Freeman, G.J., Sharpe, A.H., and Haigis, M.C. (2022). Tumor cells dictate anti-tumor immune responses by altering pyruvate utilization and succinate signaling in CD8+ T cells. Cell Metabolism *34*, 1137-1150.e6. https://doi.org/10.1016/j.cmet.2022.06.008.

77. Zhang, H., Santana-Codina, N., Yu, Q., Poupault, C., Campos, C., Qin, X., Sindoni, N., Ciscar, M., Padhye, A., Kuljanin, M., et al. (2025). De novo pyrimidine biosynthesis inhibition synergizes with BCL-XL targeting in pancreatic cancer. Nat Commun *16*, 6987. https://doi.org/10.1038/s41467-025-61242-x.

78. Halbrook, C.J., Pontious, C., Kovalenko, I., Lapienyte, L., Dreyer, S., Lee, H.-J., Thurston, G., Zhang, Y., Lazarus, J., Sajjakulnukit, P., et al. (2019). Macrophage-Released Pyrimidines Inhibit Gemcitabine Therapy in Pancreatic Cancer. Cell Metab *29*, 1390-1399.e6. https://doi.org/10.1016/j.cmet.2019.02.001.

79. Dalin, S., Sullivan, M.R., Lau, A.N., Grauman-Boss, B., Mueller, H.S., Kreidl, E., Fenoglio, S., Luengo, A., Lees, J.A., Vander Heiden, M.G., et al. (2019). Deoxycytidine Release from Pancreatic Stellate Cells Promotes Gemcitabine Resistance. Cancer Res *79*, 5723–5733. https://doi.org/10.1158/0008-5472.CAN-19-0960.

80. Egan, D.F., Chun, M.G.H., Vamos, M., Zou, H., Rong, J., Miller, C.J., Lou, H.J., Raveendra-Panickar, D., Yang, C.-C., Sheffler, D.J., et al. (2015). Small Molecule Inhibition of the Autophagy Kinase ULK1 and Identification of ULK1 Substrates. Molecular Cell *59*, 285–297. https://doi.org/10.1016/j.molcel.2015.05.031.

81. Cordes, T., and Metallo, C.M. (2019). Quantifying Intermediary Metabolism and Lipogenesis in Cultured Mammalian Cells Using Stable Isotope Tracing and Mass Spectrometry. Methods Mol Biol *1978*, 219–241. https://doi.org/10.1007/978-1-4939-9236-2_14.

82. Kuna, R.S., Kumar, A., Wessendorf-Rodriguez, K.A., Galvez, H., Green, C.R., McGregor, G.H., Cordes, T., Shaw, R.J., Svensson, R.U., and Metallo, C.M. (2023). Inter-organelle cross-talk supports acetyl-coenzyme A homeostasis and lipogenesis under metabolic stress. Science Advances *9*, eadf0138. https://doi.org/10.1126/sciadv.adf0138.

83. Adams, K.J., Pratt, B., Bose, N., Dubois, L.G., St John-Williams, L., Perrott, K.M., Ky, K., Kapahi, P., Sharma, V., MacCoss, M.J., et al. (2020). Skyline for Small Molecules: A Unifying Software Package for Quantitative Metabolomics. J Proteome Res *19*, 1447–1458. https://doi.org/10.1021/acs.jproteome.9b00640.

84. Bordi, M., De Cegli, R., Testa, B., Nixon, R.A., Ballabio, A., and Cecconi, F. (2021). A gene toolbox for monitoring autophagy transcription. Cell Death Dis *12*, 1044. https://doi.org/10.1038/s41419-021-04121-9.

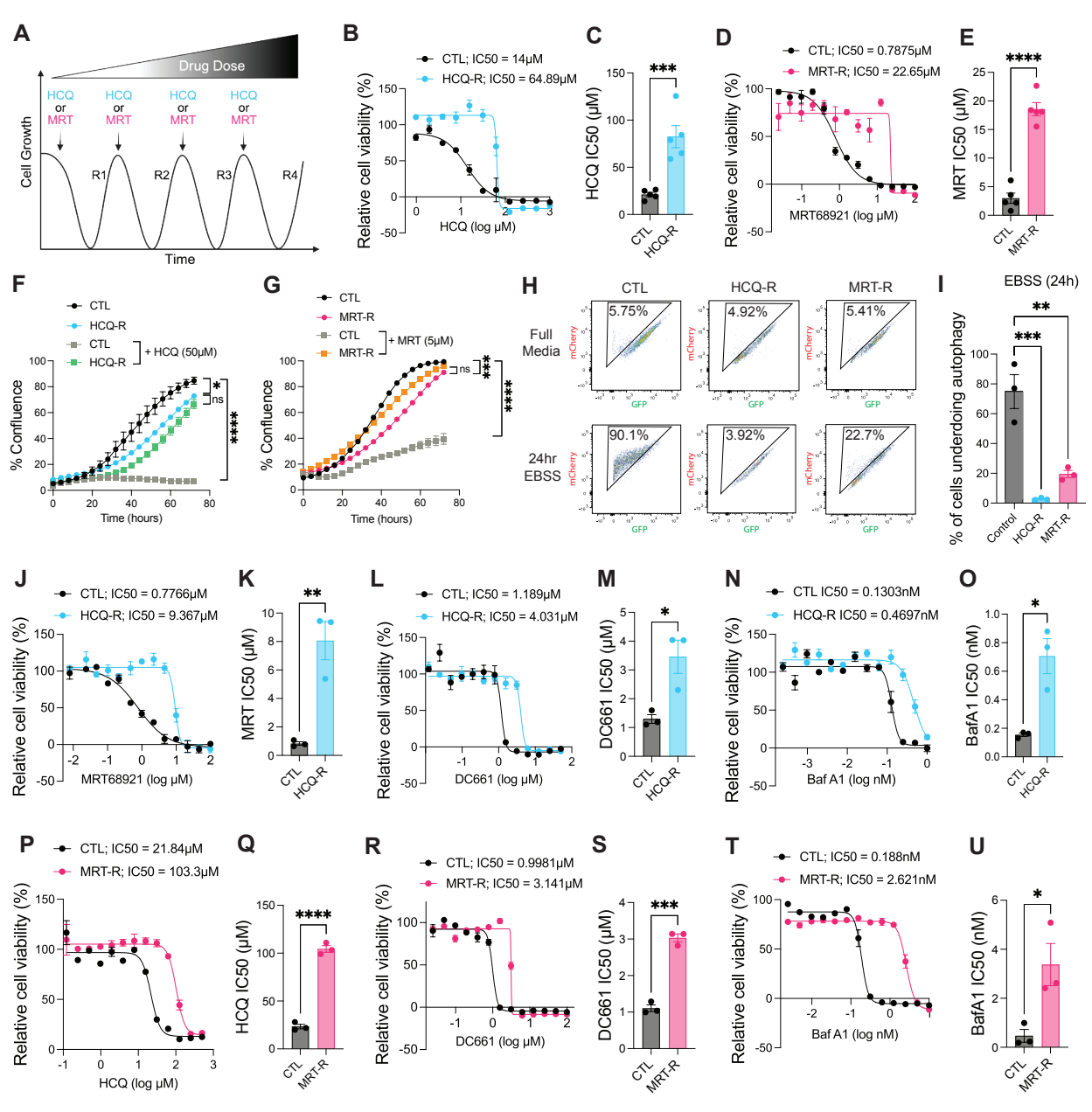
A
Drug Dose
HCQ or MRT
HCQ or MRT
HCQ or MRT
HCQ or MRT
Cell Growth
R1
R2
R3
R4
Time
B
CTL; IC50 = 14μM
HCQ-R; IC50 = 64.89μM
Relative cell viability (%)
HCQ (log μM)
C
HCQ IC50 (μM)
CTL
HCQ-R
D
CTL; IC50 = 0.7875μM
MRT-R; IC50 = 22.65μM
Relative cell viability (%)
MRT68921 (log μM)
E
MRT IC50 (μM)
CTL
MRT-R
F
CTL
HCQ-R
CTL
HCQ-R
+ HCQ (50μM)
% Confluence
Time (hours)
G
CTL
MRT-R
CTL
MRT-R
+ MRT (5μM)
% Confluence
Time (hours)
H
CTL
HCQ-R
MRT-R
Full Media
24hr EBSS
5.75%
4.92%
5.41%
90.1%
3.92%
22.7%
mCherry
GFP
I
EBSS (24h)
% of cells underdoing autophagy
Control
HCQ-R
MRT-R
J
CTL; IC50 = 0.7766μM
HCQ-R; IC50 = 9.367μM
Relative cell viability (%)
MRT68921 (log μM)
K
MRT IC50 (μM)
CTL
HCQ-R
L
CTL; IC50 = 1.189μM
HCQ-R; IC50 = 4.031μM
Relative cell viability (%)
DC661 (log μM)
M
DC661 IC50 (μM)
CTL
HCQ-R
N
CTL IC50 = 0.1303nM
HCQ-R IC50 = 0.4697nM
Relative cell viability (%)
Baf A1 (log nM)
O
BafA1 IC50 (nM)
CTL
HCQ-R
P
CTL; IC50 = 21.84μM
MRT-R; IC50 = 103.3μM
Relative cell viability (%)
HCQ (log μM)
Q
HCQ IC50 (μM)
CTL
MRT-R
R
CTL; IC50 = 0.9981μM
MRT-R; IC50 = 3.141μM
Relative cell viability (%)
DC661 (log μM)
S
DC661 IC50 (μM)
CTL
MRT-R
T
CTL; IC50 = 0.188nM
MRT-R; IC50 = 2.621nM
Relative cell viability (%)
Baf A1 (log nM)
U
BafA1 IC50 (nM)
CTL
MRT-R

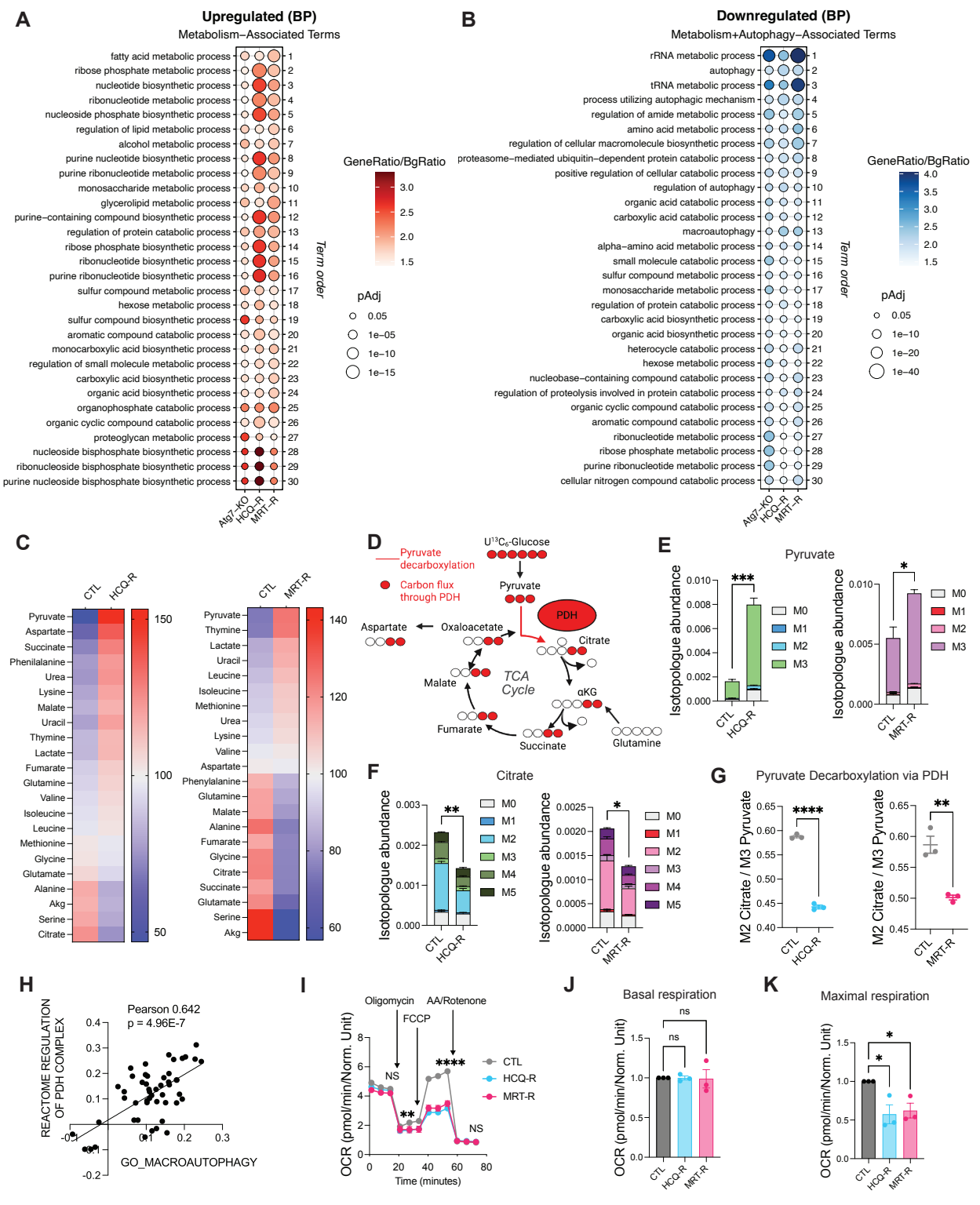
A
Upregulated (BP)
Metabolism−Associated Terms
fatty acid metabolic process
ribose phosphate metabolic process
nucleotide biosynthetic process
ribonucleotide metabolic process
nucleoside phosphate biosynthetic process
regulation of lipid metabolic process
alcohol metabolic process
purine nucleotide biosynthetic process
purine ribonucleotide metabolic process
monosaccharide metabolic process
glycerolipid metabolic process
purine−containing compound biosynthetic process
regulation of protein catabolic process
ribose phosphate biosynthetic process
ribonucleotide biosynthetic process
purine ribonucleotide biosynthetic process
sulfur compound metabolic process
hexose metabolic process
sulfur compound biosynthetic process
aromatic compound catabolic process
monocarboxylic acid biosynthetic process
regulation of small molecule metabolic process
carboxylic acid biosynthetic process
organic acid biosynthetic process
organophosphate catabolic process
organic cyclic compound catabolic process
proteoglycan metabolic process
nucleoside bisphosphate biosynthetic process
ribonucleoside bisphosphate biosynthetic process
purine nucleoside bisphosphate biosynthetic process
Term order
Atg7−KO
HCQ-R
MRT-R
GeneRatio/BgRatio
3.0
2.5
2.0
1.5
pAdj
0.05
1e−05
1e−10
1e−15
B
Downregulated (BP)
Metabolism+Autophagy−Associated Terms
rRNA metabolic process
autophagy
tRNA metabolic process
process utilizing autophagic mechanism
regulation of amide metabolic process
amino acid metabolic process
regulation of cellular macromolecule biosynthetic process
proteasome−mediated ubiquitin−dependent protein catabolic process
positive regulation of cellular catabolic process
regulation of autophagy
organic acid catabolic process
carboxylic acid catabolic process
macroautophagy
alpha−amino acid metabolic process
small molecule catabolic process
sulfur compound metabolic process
monosaccharide metabolic process
regulation of protein catabolic process
carboxylic acid biosynthetic process
organic acid biosynthetic process
heterocycle catabolic process
hexose metabolic process
nucleobase−containing compound catabolic process
regulation of proteolysis involved in protein catabolic process
organic cyclic compound catabolic process
aromatic compound catabolic process
ribonucleotide metabolic process
ribose phosphate metabolic process
purine ribonucleotide metabolic process
cellular nitrogen compound catabolic process
Term order
Atg7−KO
HCQ-R
MRT-R
GeneRatio/BgRatio
4.0
3.5
3.0
2.5
2.0
1.5
pAdj
0.05
1e−10
1e−20
1e−40
C
CTL
HCQ-R
Pyruvate
Aspartate
Succinate
Phenilalanine
Urea
Lysine
Malate
Uracil
Thymine
Lactate
Fumarate
Glutamine
Valine
Isoleucine
Leucine
Methionine
Glycine
Glutamate
Alanine
Akg
Serine
Citrate
150
100
50
CTL
MRT-R
Pyruvate
Thymine
Lactate
Uracil
Leucine
Isoleucine
Methionine
Urea
Lysine
Valine
Aspartate
Phenylalanine
Glutamine
Malate
Alanine
Fumarate
Glycine
Citrate
Succinate
Glutamate
Serine
Akg
140
120
100
80
60
D
Pyruvate decarboxylation
Carbon flux through PDH
U13C6-Glucose
Pyruvate
PDH
Aspartate
Oxaloacetate
Citrate
Malate
TCA Cycle
αKG
Fumarate
Succinate
Glutamine
E
Pyruvate
Isotopologue abundance
0.010
0.008
0.006
0.004
0.002
0.000
***
CTL
HCQ-R
M0
M1
M2
M3
Isotopologue abundance
0.010
0.005
0.000
*
CTL
MRT-R
M0
M1
M2
M3
F
Citrate
Isotopologue abundance
0.003
0.002
0.001
0.000
**
CTL
HCQ-R
M0
M1
M2
M3
M4
M5
Isotopologue abundance
0.0025
0.0020
0.0015
0.0010
0.0005
0.0000
*
CTL
MRT-R
M0
M1
M2
M3
M4
M5
G
Pyruvate Decarboxylation via PDH
M2 Citrate / M3 Pyruvate
0.65
0.60
0.55
0.50
0.45
0.40
****
CTL
HCQ-R
M2 Citrate / M3 Pyruvate
0.65
0.60
0.55
0.50
0.45
**
CTL
MRT-R
H
Pearson 0.642
p = 4.96E-7
REACTOME REGULATION OF PDH COMPLEX
0.4
0.3
0.2
0.1
-0.1
-0.2
-0.1
0.1
0.2
0.3
GO_MACROAUTOPHAGY
I
Oligomycin
FCCP
AA/Rotenone
OCR (pmol/min/Norm. Unit)
6
4
2
0
NS
**
****
NS
CTL
HCQ-R
MRT-R
0
20
40
60
80
Time (minutes)
J
Basal respiration
OCR (pmol/min/Norm. Unit)
1.5
1.0
0.5
0.0
ns
ns
CTL
HCQ-R
MRT-R
K
Maximal respiration
OCR (pmol/min/Norm. Unit)
1.5
1.0
0.5
0.0
*
*
CTL
HCQ-R
MRT-R

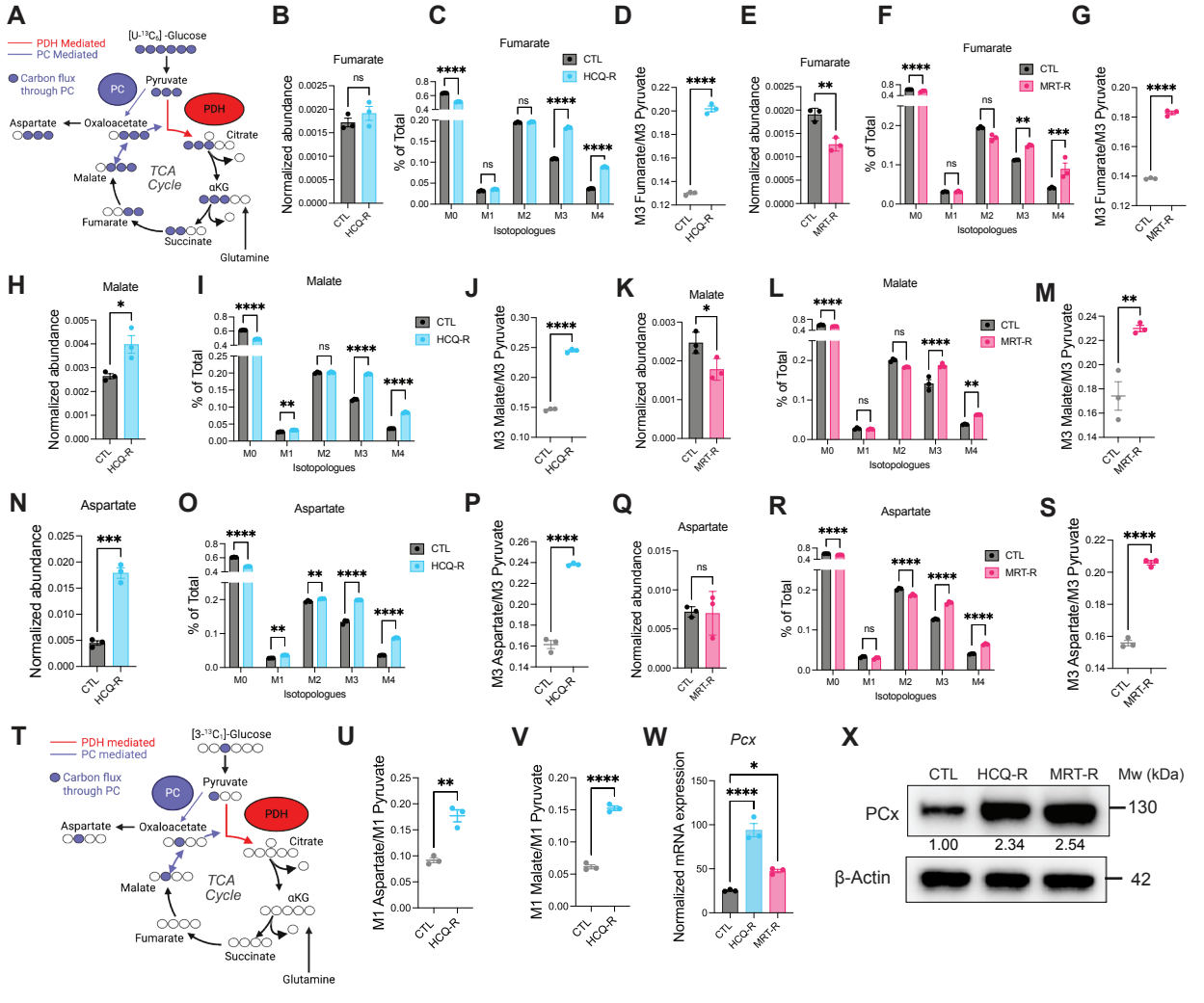
A
PDH Mediated
PC Mediated
Carbon flux through PC
[U-13C6] -Glucose
Pyruvate
PC
PDH
Aspartate
Oxaloacetate
Citrate
Malate
TCA Cycle
αKG
Fumarate
Succinate
Glutamine
B
Fumarate
Normalized abundance
ns
CTL
HCQ-R
C
Fumarate
% of Total
CTL
HCQ-R
Isotopologues
D
M3 Fumarate/M3 Pyruvate
E
Fumarate
Normalized abundance
MRT-R
F
Fumarate
% of Total
MRT-R
G
M3 Fumarate/M3 Pyruvate
H
Malate
Normalized abundance
I
Malate
% of Total
J
M3 Malate/M3 Pyruvate
K
Malate
Normalized abundance
L
Malate
% of Total
M
M3 Malate/M3 Pyruvate
N
Aspartate
Normalized abundance
O
Aspartate
% of Total
P
M3 Aspartate/M3 Pyruvate
Q
Aspartate
Normalized abundance
R
Aspartate
% of Total
S
M3 Aspartate/M3 Pyruvate
T
PDH mediated
PC mediated
Carbon flux through PC
[3-13C1]-Glucose
Pyruvate
PC
PDH
Aspartate
Oxaloacetate
Citrate
Malate
TCA Cycle
αKG
Fumarate
Succinate
Glutamine
U
M1 Aspartate/M1 Pyruvate
V
M1 Malate/M1 Pyruvate
W
Pcx
Normalized mRNA expression
X
CTL
HCQ-R
MRT-R
Mw (kDa)
PCx
130
1.00
2.34
2.54
β-Actin
42

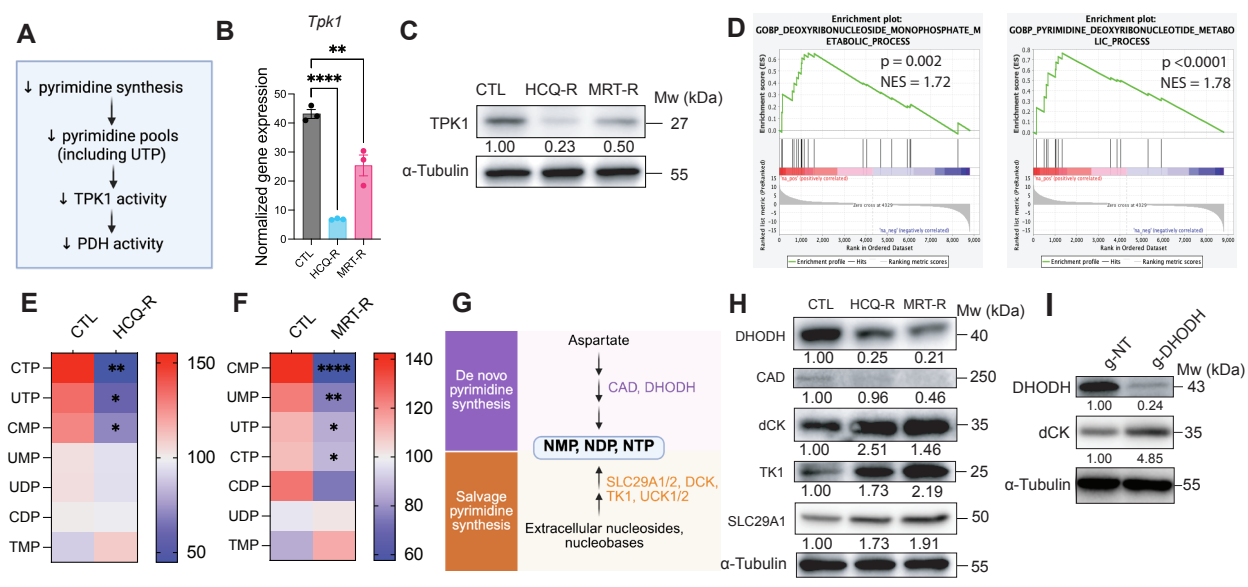
A
↓ pyrimidine synthesis
↓ pyrimidine pools (including UTP)
↓ TPK1 activity
↓ PDH activity
B
Tpk1
Normalized gene expression
CTL
HCQ-R
MRT-R
C
CTL HCQ-R MRT-R
Mw (kDa)
TPK1
27
1.00 0.23 0.50
α-Tubulin
55
D
Enrichment plot: GOBP_DEOXYRIBONUCLEOSIDE_MONOPHOSPHATE_METABOLIC_PROCESS
p = 0.002
NES = 1.72
Enrichment plot: GOBP_PYRIMIDINE_DEOXYRIBONUCLEOTIDE_METABOLIC_PROCESS
p <0.0001
NES = 1.78
E
CTL HCQ-R
CTP UTP CMP UMP UDP CDP TMP
F
CTL MRT-R
CMP UMP UTP CTP CDP UDP TMP
G
De novo pyrimidine synthesis
Salvage pyrimidine synthesis
Aspartate
CAD, DHODH
NMP, NDP, NTP
SLC29A1/2, DCK, TK1, UCK1/2
Extracellular nucleosides, nucleobases
H
CTL HCQ-R MRT-R
Mw (kDa)
DHODH 40 1.00 0.25 0.21
CAD 250 1.00 0.96 0.46
dCK 35 1.00 2.51 1.46
TK1 25 1.00 1.73 2.19
SLC29A1 50 1.00 1.73 1.91
α-Tubulin 55
I
g-NT g-DHODH
Mw (kDa)
DHODH 43 1.00 0.24
dCK 35 1.00 4.85
α-Tubulin 55

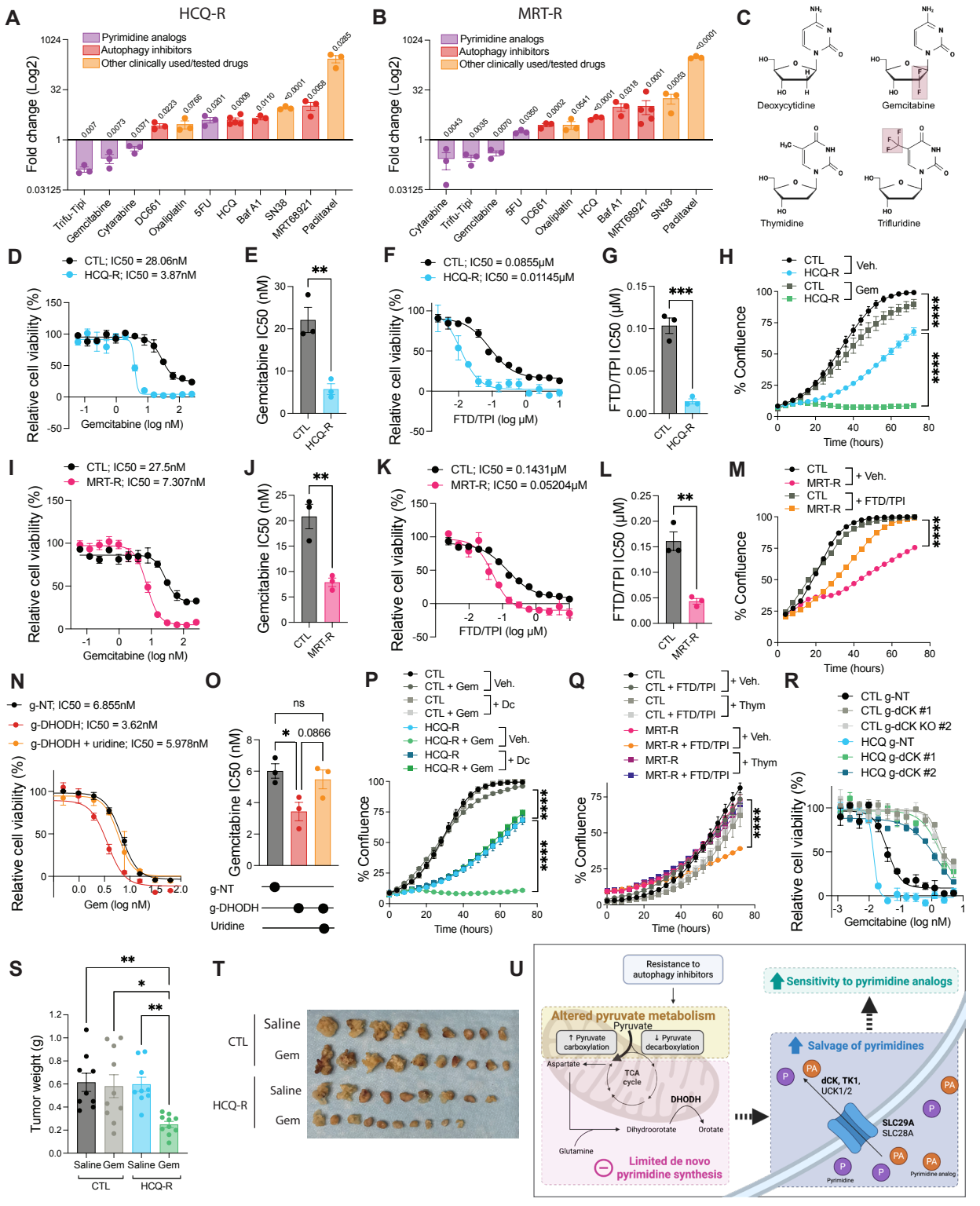
A
HCQ-R
Pyrimidine analogs
Autophagy inhibitors
Other clinically used/tested drugs
Fold change (Log2)
1024
32
1
0.03125
0.007
0.0073
0.0371
0.0223
0.0766
0.0231
0.0039
0.0110
<0.0001
0.0056
0.0285
Trifu-Tipi
Gemcitabine
Cytarabine
DC661
Oxaliplatin
5FU
HCQ
Baf A1
SN38
MRT68921
Paclitaxel
B
MRT-R
Pyrimidine analogs
Autophagy inhibitors
Other clinically used/tested drugs
Fold change (Log2)
1024
32
1
0.03125
0.0043
0.0035
0.0070
0.0350
0.0002
0.0541
<0.0001
0.0318
0.0001
0.0053
<0.0001
Cytarabine
Trifu-Tipi
Gemcitabine
5FU
DC661
Oxaliplatin
HCQ
Baf A1
MRT68921
SN38
Paclitaxel
C
Deoxycytidine
Gemcitabine
Thymidine
Trifluridine
D
CTL; IC50 = 28.06nM
HCQ-R; IC50 = 3.87nM
Relative cell viability (%)
Gemcitabine (log nM)
E
Gemcitabine IC50 (nM)
**
CTL
HCQ-R
F
CTL; IC50 = 0.0855μM
HCQ-R; IC50 = 0.01145μM
Relative cell viability (%)
FTD/TPI (log μM)
G
FTD/TPI IC50 (μM)
***
CTL
HCQ-R
H
CTL
HCQ-R
Veh.
CTL
HCQ-R
Gem
% Confluence
Time (hours)
****
****
I
CTL; IC50 = 27.5nM
MRT-R; IC50 = 7.307nM
Relative cell viability (%)
Gemcitabine (log nM)
J
Gemcitabine IC50 (nM)
**
CTL
MRT-R
K
CTL; IC50 = 0.1431μM
MRT-R; IC50 = 0.05204μM
Relative cell viability (%)
FTD/TPI (log μM)
L
FTD/TPI IC50 (μM)
**
CTL
MRT-R
M
CTL
MRT-R
+ Veh.
CTL
MRT-R
+ FTD/TPI
% Confluence
Time (hours)
****
N
g-NT; IC50 = 6.855nM
g-DHODH; IC50 = 3.62nM
g-DHODH + uridine; IC50 = 5.978nM
Relative cell viability (%)
Gem (log nM)
O
ns
*
0.0866
Gemcitabine IC50 (nM)
g-NT
g-DHODH
Uridine
P
CTL
CTL + Gem
Veh.
CTL
CTL + Gem
+ Dc
HCQ-R
HCQ-R + Gem
Veh.
HCQ-R
HCQ-R + Gem
+ Dc
% Confluence
Time (hours)
****
****
Q
CTL
CTL + FTD/TPI
+ Veh.
CTL
CTL + FTD/TPI
+ Thym
MRT-R
MRT-R + FTD/TPI
+ Veh.
MRT-R
MRT-R + FTD/TPI
+ Thym
% Confluence
Time (hours)
****
R
CTL g-NT
CTL g-dCK #1
CTL g-dCK KO #2
HCQ g-NT
HCQ g-dCK #1
HCQ g-dCK #2
Relative cell viability (%)
Gemcitabine (log nM)
S
**
*
**
Tumor weight (g)
Saline
Gem
Saline
Gem
CTL
HCQ-R
T
CTL
Saline
Gem
HCQ-R
Saline
Gem
U
Resistance to autophagy inhibitors
Sensitivity to pyrimidine analogs
Altered pyruvate metabolism
Pyruvate
↑ Pyruvate carboxylation
↓ Pyruvate decarboxylation
Aspartate
TCA cycle
DHODH
Dihydroorotate
Orotate
Glutamine
Limited de novo pyrimidine synthesis
Salvage of pyrimidines
dCK, TK1, UCK1/2
SLC29A
SLC28A
Pyrimidine
Pyrimidine analog

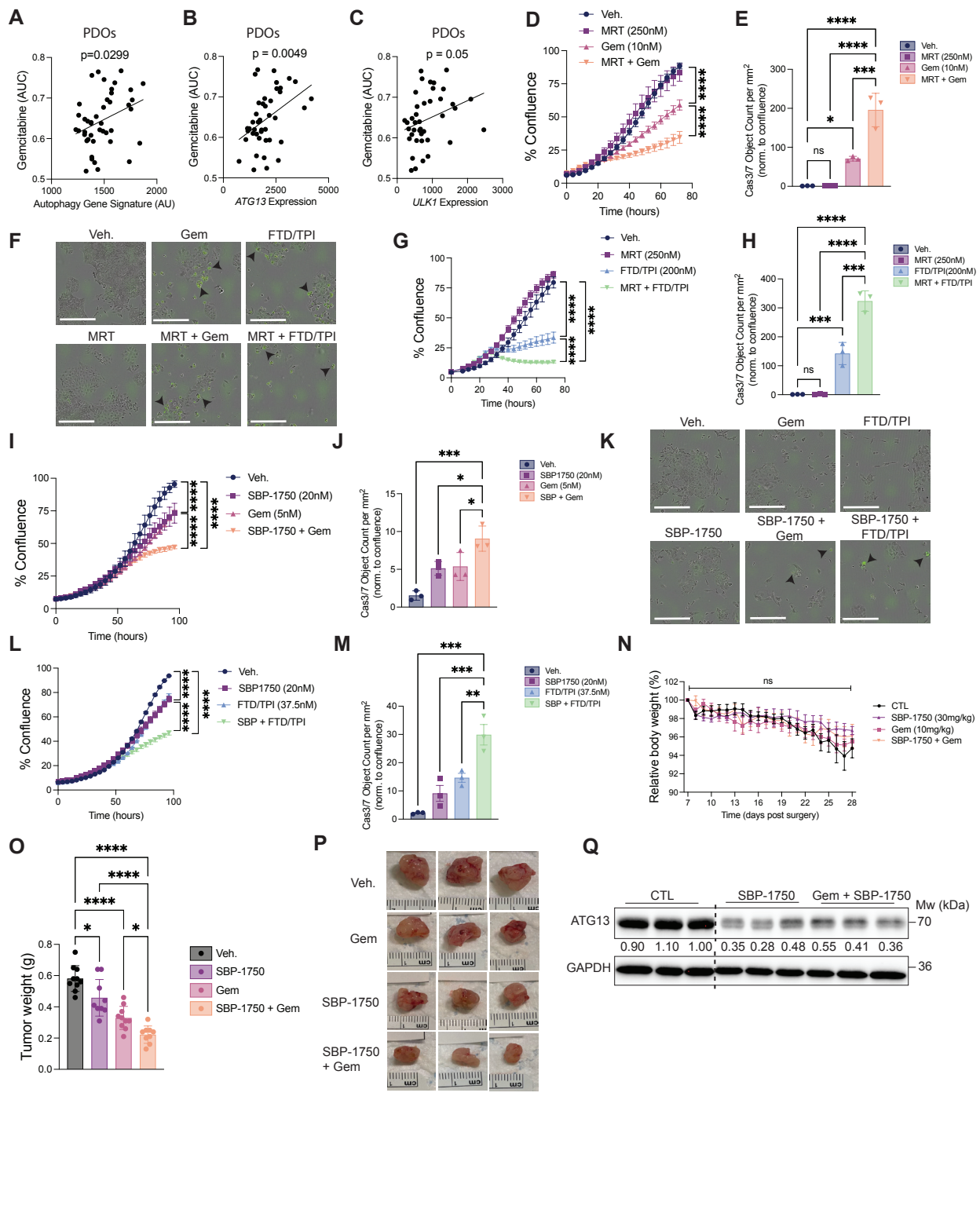
A
PDOs
p=0.0299
Gemcitabine (AUC)
Autophagy Gene Signature (AU)
B
PDOs
p = 0.0049
Gemcitabine (AUC)
ATG13 Expression
C
PDOs
p = 0.05
Gemcitabine (AUC)
ULK1 Expression
D
Veh.
MRT (250nM)
Gem (10nM)
MRT + Gem
% Confluence
Time (hours)
E
Cas3/7 Object Count per mm2 (norm. to confluence)
Veh.
MRT (250nM)
Gem (10nM)
MRT + Gem
ns
F
Veh.
Gem
FTD/TPI
MRT
MRT + Gem
MRT + FTD/TPI
G
Veh.
MRT (250nM)
FTD/TPI (200nM)
MRT + FTD/TPI
% Confluence
Time (hours)
H
Cas3/7 Object Count per mm2 (norm. to confluence)
Veh.
MRT (250nM)
FTD/TPI(200nM)
MRT + FTD/TPI
ns
I
Veh.
SBP-1750 (20nM)
Gem (5nM)
SBP-1750 + Gem
% Confluence
Time (hours)
J
Cas3/7 Object Count per mm2 (norm. to confluence)
Veh.
SBP1750 (20nM)
Gem (5nM)
SBP + Gem
K
Veh.
Gem
FTD/TPI
SBP-1750
SBP-1750 + Gem
SBP-1750 + FTD/TPI
L
Veh.
SBP1750 (20nM)
FTD/TPI (37.5nM)
SBP + FTD/TPI
% Confluence
Time (hours)
M
Cas3/7 Object Count per mm2 (norm. to confluence)
Veh.
SBP1750 (20nM)
FTD/TPI (37.5nM)
SBP + FTD/TPI
N
Relative body weight (%)
ns
CTL
SBP-1750 (30mg/kg)
Gem (10mg/kg)
SBP-1750 + Gem
Time (days post surgery)
O
Tumor weight (g)
Veh.
SBP-1750
Gem
SBP-1750 + Gem
P
Veh.
Gem
SBP-1750
SBP-1750 + Gem
Q
CTL
SBP-1750
Gem + SBP-1750
Mw (kDa)
ATG13
70
0.90 1.10 1.00 0.35 0.28 0.48 0.55 0.41 0.36
GAPDH
36